

Characterization and Implications of Solids Associated with Hydraulic Fracturing Flowback and
Produced Water from the Duvernay Formation, Alberta, Canada

Shannon L. Flynn^{1,2*}, Konstantin von Gunten², Tyler Warchola², Katherine Snihur², Tori Z.
Forbes³, Greg G. Goss⁴, Murray K. Gingras², Kurt O. Konhauser², and Daniel S. Alessi².

¹*School of Natural and Environmental Sciences,
Newcastle University, Newcastle upon Tyne, NE1 7RU, UK*

²*Department of Earth and Atmospheric Sciences,
University of Alberta, Edmonton, AB T6G 2E3, Canada*

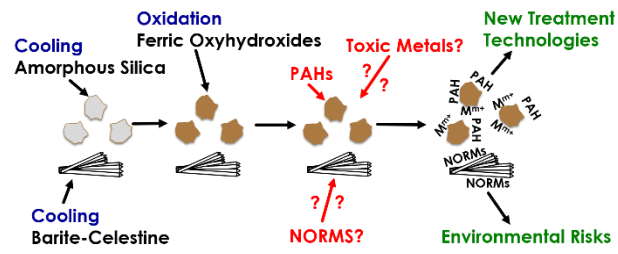
³*Department of Chemistry
University of Iowa, Iowa City, IA, 52242, USA*

⁴*Department of Biological Sciences,
University of Alberta, Edmonton, AB T6G 2E3, Canada*

* Corresponding Author: shannon.flynn@ncl.ac.uk

Abstract:

Public concern is heightened around flowback and produced water (FPW) generated by the hydraulic fracturing process. FPW is a complex mix of organic and inorganic solutes derived from both the injected hydraulic fracturing fluid and interactions with the subsurface lithology. Few studies to date have systematically investigated the composition of FPW or its individual components. Here, we provide the first systematic characterization of the composition of the solids associated with FPW by analyzing samples from three wells drilled into the Duvernay Formation in Alberta, Canada. The FPW initially returned to the surface with high total dissolved solids (greater than 170,000 mg/L) and enriched with Fe(II), silica, sulfate, barium, and strontium. The solids form two distinct phases once the FPW reached the surface: (1) silica-enriched Fe(III) oxyhydroxides, and (2) a barite-celestine solid solution. We hypothesize that the precipitation of the amorphous silica-enriched Fe(III) oxyhydroxide is a two-step process, where first the silica precipitates as a function of the cooling of the FPW from elevated subsurface temperatures to ambient surface temperatures. Next, the silica acts as a template for the precipitation of Fe(III) oxyhydroxide as the diffusion of oxygen into the subsurface causes oxidation of aqueous Fe(II). The barite-celestine solid solution precipitates solely as a function of cooling. Elevated dissolved Fe concentrations in FPW and modeled saturation indices from five North American shale plays (Marcellus, Fayetteville, Barnett, Bakken, and Denver-Julesburg) indicates that solids similar to those found in Duvernay FPW, specifically Fe(III) oxyhydroxides, barite and quartz, are likely to occur. With the solids known to carry a significant portion of FPW's toxicity and organic contaminant load¹, the development of new treatment technologies, such as the oxidation of the Fe(II) in FPW, may increase FPW reuse and reduce the environmental risk posed by FPW.



40

41 Key Words

42 Hydraulic fracturing, Flowback and produced waters, Iron-oxides, Treatment

43

1 Introduction

Hydraulic fracturing for oil and gas extraction has generated a range of environmental concerns including air pollution², induced seismicity³⁻⁵, fresh water allocations⁶⁻⁸, drinking water contamination⁹⁻¹⁰, and human health risks¹¹⁻¹³. While there has been substantial public concern on the potential for fluids related to hydraulic fracturing migrating to the shallow subsurface and contaminating groundwater, the most likely routes for groundwater contamination are the loss of wellbore integrity or surface spills during the handling and transport of hydraulic fracturing fluid (HFF) or flowback and produced waters (FPW)^{9,14-18}.

Much of our current understanding of the composition of FPW comes from just a few locations, namely the Marcellus Formation (Northeast USA)¹⁹⁻²¹, Julesburg basin (Colorado, USA)²²⁻²³, Duvernay Formation (Alberta, Canada)¹, and Horn River Formation (British Columbia, Canada)²⁴. Generally, FPW has been found to contain high total dissolved solids (TDS), ranging from 10,000 to over 300,000 mg/L depending on the formation, fracturing process, and time. The TDS is largely composed of Na and Cl, with elevated concentrations of Ca, Fe, Mg, and Sr²⁰⁻²⁴. Trace elements, such as Se, As, Ba¹⁹, and naturally occurring radioactive materials (NORMs)²⁵⁻²⁶, have also been documented in FPW.

The organic chemical composition of FPW is also complex. FPW is composed not only of the hydrocarbons naturally present in the target geologic formation, but also HFF chemicals and the compounds that form as a product of secondary reactions when HFF is exposed to elevated subsurface temperatures and pressures^{1,27}. As FPW can contain numerous combinations of the thousands of chemicals known to have been used in hydraulic fracturing fluids alone¹³, targeted analysis can be difficult. To date, a variety of compounds have been either identified or

quantified in FPW, including volatile organic compounds (e.g., benzene, toluene, ethylbenzene, and xylene)²⁷⁻²⁹, polymers (e.g., polyethylene glycols and polypropylene glycols)³⁰⁻³², biocides (e.g., glutaraldehyde and alkyl dimethyl benzyl ammonium chloride: Ferrer and Thurman, 2015), surfactants (e.g., dimethylamines, cocamidopropyl and its derivatives)³³, and reaction byproducts (e.g., halogenated methanes and acetones, chloromethyls, delayed acids, and organophosphates)^{1,27}.

FPW compositional studies have focused the analysis primarily on the fraction that passes through a membrane (0.2 or 0.45 μm), i.e., the dissolved phase. With the exception of a few filtration studies³⁴⁻³⁷, such as Phan et al.³⁸ who examined the composition of colloidal fractions that passed through 0.45 μm pore filters, the associated solid and colloidal fractions that do not pass through the filters have been largely ignored. This is problematic because in previously studied contaminated aquifers, colloidal fractions are a major vector for the transport for contaminants, such as uranium³⁹⁻⁴⁰, plutonium⁴¹⁻⁴², and polycyclic aromatic hydrocarbons (PAHs)⁴³⁻⁴⁴. Indeed, recent work has demonstrated strong links between the FPW solids, PAHs and environmental toxicity^{1,45-46}. Specifically, He et al.¹ showed that zebrafish (*Danio rerio*) embryos exposed to unfiltered FPW samples had approximately double the ethoxyresorufin-O-deethylase (EROD) activity compared to those exposed to the corresponding filtered samples. Additionally, the 96 h LC₅₀ concentration for samples containing solids was approximately 50% lower than the corresponding samples without solids. Further, He et al.⁴⁵ found a significant increase in EROD activity and thiobarbituric acid reactive substances in gill, kidney and liver tissues of juvenile rainbow trout (*Oncorhynchus mykiss*) when FPW solids were present. The exact mechanisms by which the solids cause the increased toxicity has yet to be determined,

including whether the toxicity is derived primarily from the solids themselves or the associated organic compounds.

In this study, we have characterized the chemical composition and mineralogy of FPW associated solids from the Duvernay Formation. The Duvernay Formation is a Devonian-aged formation composed of silt-sized quartz, mica, K-feldspar, and plagioclase; the clay-size fraction is dominantly quartz and calcite with subordinate clay illite/smectite and less abundant kaolinite in descending order of their relative abundance^{47,48} (for more information, a full description of the geologic context is provided in the Supplemental Information). Using the FPW data we model the saturation indices for the minerals identified in the characterization of the solids and then discuss the mechanisms underpinning their formation with a comparison to the potential for secondary mineral formation in five other North American shale plays. Analysis of bulk chemistry of aqueous and solid phases capture on 0.2 μm membranes were conducted, and particle morphology and spot elemental and mineralogy of the solids were determined using spectroscopy. 0.2 μm membranes were selected as it has been suggested that 0.2 or 0.45 μm are the most commonly used pore sizes used microfiltration for FPW reuse⁴⁹. The strong correlations observed between toxicity, oxidative stress, endocrine disruption, and the FPW solids^{1,45} indicates the importance of characterizing these solids. Insights into their composition and formation will improve the handling, treatment, and disposal technologies to mitigate risks.

2 Methods

2.1 Flowback Samples

Samples of FPW from three hydraulically fractured wells located near Fox Creek, Alberta, Canada in the Devonian-aged Duvernay Formation were acquired from Encana Corporation. All samples were collected after the oil and gas separator into polypropylene buckets. Sample 1 (S1) was collected 7 days after the initiation of the flowback and collected in August 2014, which was previously examined for aqueous toxicity and characterized in He et al.^{1,45}. Sample 2 (S2) collected 10 days after the initiation of the flowback and collected in November 2015⁴⁷. Sample 3 (S3) from 24 hrs after the initiation of the flowback and collected in October 2016. Upon arrival the pH of each fluid was measured using a Mettler Toledo Easy Five dual pH meter, which was calibrated using a 3 point calibration method using buffers pH 4.01, 7.00, 10.01. The buffers were not matched to the ionic strength of the FPW and there for should be viewed as an estimate. A portion of S3 was further treated by vigorously bubbling it with air for 4 hours, subsequently referred to as S3_Ox.

2.2 X-ray Diffraction Spectroscopy

Two samples of Duvernay shale collected as drill cuttings from 700 m apart along the horizontal bore of the hydraulic fractured well from which S3 were acquired were analyzed for their bulk mineral composition (Figure SI.1). Samples were soaked for 1 hrs in with Optima™ grade n-Hexane at a ratio of 10mL solvent to 0.5g sample to remove residual drilling fluid organic compounds. The cuttings were recovered by centrifugation and then the remaining solvent was allowed to evaporate before analysis. Bulk mineralogy was determined using X-ray diffraction (XRD) using a Rigaku Ultima IV. A Co-60 electron tube radioactive source and a scan rate of 2q/min with a step size of 0.02q were used, spectra was then fit using JADE 9 software and ICDD (International Centre for Diffraction Data) and ICSD (Inorganic Crystal Structure Database).

2.3 Digestions

Samples of FPW solids for digestion were prepared using a method similar to He et al.¹. Each of the three FPW samples were thoroughly shaken before being passed through a nylon membrane filter with a nominal pore size of 0.2 μm . The solids retained by the filter were then rinsed with 18M Ω ultrapure water while still on the filter, then covered and air dried for 48 h at room temperature.

The bulk elemental composition of the FPW solids was determined by alkaline fusion digestion performed in triplicate using a method similar to that described by GBC Scientific Equipment⁵¹. Alkaline fusion digestions were chosen over hydrofluoric acid digests due to the potential for the loss of Si from the evaporation of SiF_4 and SiF_6 and the precipitation of Al, Fe, Sr fluoride minerals in hydrofluoric acid digestions. Additionally, von Gunten et al.⁵² found alkaline fusion and hydrofluoric digestions to yield comparable results for total digestions. For each, 1.5 g of NaOH was melted in a nickel crucible over a Bunsen burner, and then 0.1 g of sample was added to the melt with 0.5 g of Na_2O_2 and an additional 0.5 g of NaOH. The crucibles were then covered with nickel covers and heated for an additional 5 minutes. After cooling, the crucibles were rinsed with 6 M HCl before being placed into a polypropylene beaker along with the lid. Aliquots of 6 M HCl were added until all the remaining particles dissolved (approximately 20-30 mL), the final the volume was adjusted to 100 ml with 18 M Ω ultrapure water. Solutions were diluted 10-fold with a mixture containing 2% HNO_3 and 0.5% HCl prior to analysis by ICP-MS/MS (see Section 2.3.1). Metal recoveries were verified using STSD-3 reference material (CANMET Mining and Mineral Sciences Laboratories), which was digested in parallel to the samples.

2.4 Aqueous Analysis

The aqueous phase of samples S1 and S2 were previously analyzed and reported in He et al.¹ and Blewett et al.⁵⁰, respectively. For S3 and all aqueous phase analyses, the samples were vigorously shaken before an aliquot was removed and filtered through a 0.2 µm nylon membrane filter into polypropylene ICP tubes. The filtrate was then used for all subsequent analyses.

2.4.1 ICP-MS Analysis

The aqueous phase of S3 and digestion solutions from S1-3 and S3_Ox were analyzed using an Agilent 8800 ICP-MS/MS. S3 was diluted with 18 MΩ ultrapure water with a dilution factor (DF) of 850 for Na analysis and 85 for all other elements. After dilution, S3 was acidified with 12 µL of trace metal grade nitric acid per 10 mL of sample and all blanks were prepared in a similar manner with the sample fraction being replaced with 18 MΩ ultrapure water. During analysis, the RF power was set to 1550 W and the reflected power was 18 W. Samples were aspirated with a micromist nebulizer and nickel/copper cones were used. MS/MS mode was used for sample analysis to acquire greater mass resolution, and the gas collision/reaction cell was utilized with either He, O₂ or H₂ gas depending on the element. To account for instrumental drift, a standard solution of 0.5 ppm indium (In) was added to each sample utilizing an inline addition system.

2.4.2 Ion Chromatography

Ion chromatography was used to determine the chloride (Cl⁻) and sulfate (SO₄⁻²) concentrations of S3. Filtered samples were diluted 1:2000 with 18 MΩ ultrapure water and then analyzed using a Dionex Ion chromatography DX 600 with a 4mm analytical column (AS9-HC), guard column (AG9-HC), and a 4 mm ASRS Ultra suppressor.

2.4.3 Total Organic Carbon and Total Nitrogen Analysis

Total organic carbon (TOC) and total nitrogen (TN) were determined using a Shimadzu model TOC-V-CHS/CSN TOC analyzer. TOC was measured as nonpurgeable organic carbon. TN was measured as NO₂ after the sample was combusted.

2.4.4 Alkalinity Measurements

The alkalinity was determined for S1- S3 upon arrival from the field through an end-point titration to pH 4.5 in which 50 mL of FPW was titrated with 0.1 M HCl using a Metrohm Titrando 905. The milliequivalents (meq) of acid required to lower the pH was used to calculate the total alkalinity of the sample as ppm of CO₃²⁻.

2.4.5 Iron (II) Analysis

The concentration of Fe(II) was determined using the ferrozine assay as described in Porsch and Kappler⁵³. In summary, 400 µL of 1 M HCl was added to 100 µL of each sample, followed by an additional 500 µL of 0.1% by weight ferrozine. Samples were allowed to react for 5 min in the dark before spectrophotometric analysis at 562 nm using an Evolution 60S UV-Vis Spectrophotometer (Thermo Scientific). External calibration standards were prepared using Fe(II) ammonium sulfate to cover a range of 0.05-55 ppm Fe(II). Samples were diluted as needed to be within the calibration range.

2.5 Microscopy

2.5.1 Scanning Electron Microscopy (SEM)

A portion of the solids from each sample collected for digestion were set aside for imaging. Samples were then added to SEM tabs using carbon tape by dabbing the tab and tape onto the

filters. Imaging was performed using a Zeiss Sigma 300 VP-FESEM in variable pressure mode with energy dispersive X-ray spectroscopy (EDS) with dual silicon detectors, each with 60 mm² of surface area and having a resolution of 123 eV. For better resolution of particle morphologies, the samples were subsequently carbon coated using a Nanotek SEMprep 2 sputter coater before reanalysis in high resolution mode under high vacuum.

2.5.2 Transmission Electron Microscopy (TEM) with EDS and selected area electron diffraction (SAED)

The solids from S1 were suspended in 18M Ω ultrapure water at a concentration of approximately 1 mg/L. The suspension was then drop cast onto a 400 mesh carbon-coated copper grid (Pacific Grid Tech), then air dried. Imaging was conducted using a FEI Titan 80-300 TEM operating at 80 and 200 kV with point-to-point resolution of 0.19 nm and a single tilt sample holder capable of rotating from -30 to 30°. Elemental analysis was performed using an Oxford INCA 30 mm² LN₂ EDS detector with a 130 eV energy resolution, along with SAED.

2.5.3 Scanning Transmission Electron Microscopy (STEM)

A 1 g/L suspension of the solids from S1 was placed on ultra-thin carbon-coated copper grids. Excess water was removed with paper filters and the residual was evaporated under a stream of N₂ gas. TEM analysis was then conducted using a JEOL JEM-ARM200CF Atomic Resolution S/TEM at the NanoFAB facility at the University of Alberta. Scanning transmission electron microscopy (STEM) coupled to energy-dispersive X-ray spectroscopy (EDX) was done to localize particles of interest and to generate elemental maps. Transmission electron microscopy (TEM) and selected area electron diffraction (SAED) was then performed on selected particles with a camera length of 60 cm. SAED patterns were analyzed following the manufacturer's

instructions. Specifically, the distance (in pixel) of diffraction peaks to the center beam and d-spacing was measured using the Gatan Microscopy Suite Software.

3 Results and Discussion

3.1 Aqueous Chemistry

The TDS was found to range from 171,000 to 243,000 ppm, with the primarily solutes for all three samples comprising Na and Cl (85-97%). While the TDS is known to generally increase with time after FPW has started^{19, 20, 22, 23}, the TDS of S3 was composed of the highest percentage of Na and Cl (97%) and was within 6% of S2 (91%) even though S2 was collected 9 days later. This indicates that variables, such as shut-in time and the use of recycled FPW for the mixing of HFF, effects the temporal variation of FPW's composition. The higher fractions of Na and Cl in sample S3 was likely due to approximately 10% of the makeup fluid for the HFF used to fracture well S3 being recycled FPW from other wells. Other major elements (those greater than 0.5%) were Ca, K, and Sr, descending order of their relative concentration. Trace elements (those less than 0.5%) Br, Li, Mg, Mn, B, Zn, Ba, and S were detected in every sample (Table 1). Aqueous Si was only detected in S1, which is not unexpected given the low solubility of Si minerals at room temperature, including amorphous silica^{54,55}. The presence of Ba in the FPW is likely related to the dissolution of barite or desorption from aluminosilicate clays as has been suggested by Renock et al.⁵⁶ into the fracturing fluids. Sr in the FPW is likely linked to a combination of inclusions in carbonates and barite, in addition to desorption from clays much like Ba. Further investigation and leaching studies would be required to full understand the distributions of Ba and Sr and their subsequent mobilization. Silica could come from a variety of sources including the dissolution of quartz in the formation or the sand used as proppants. The elevated subsurface

temperatures are likely not great enough on their own to explain the aqueous Si concentrations, and likely it, in combination with the complexation of Si with organic matter, plays a critical role in the dissolution of the quartz as has been observed in room temperature systems^{57,58}.

The total organic carbon (TOC) concentration was the highest in S2 at 737 ppm, which was more than double S3 at 294 ppm and S1 at 212 ppm. As observed by He et al.¹ for S1, the total nitrogen (TN) was higher than TOC for S3 at 410 ppm; however, this was not observed in S2 at 425 ppm (Table 1). The relatively lower TOC than TN is likely due to most organic compounds in the samples being associated with an immiscible phase that floated on top of the aqueous samples, and which was, therefore, not collected by the autosampler during analysis¹.

The presence and persistence of aqueous Fe(II) found in S3 (254 ppm) and S1 (35.7 ppm) indicates that either weak or transient oxidizing conditions exist in the subsurface through the introduction of HFF. It is unclear whether all the Fe(II) mobilized during fracturing returns to the surface or only a portion that is the residual remains after the precipitation of Fe(III) minerals that result from the subsurface oxidation of the mobilized Fe(II), as suggested by Jew et al.⁵⁹. The fact that Fe(II) has been found in the FPW suggests that the reducing conditions were reestablished in the subsurface post fracturing. The most likely source of Fe is pyrite as experiments with Marcellus shale materials under hydraulic fracturing temperatures and pressures have found a correlation between the mobilization of Fe and the initial pyrite content of the shale used in the experiment⁴⁹. Additionally, leaching experiments on Horn River Formation shales (British Columbia, Canada) with DI water in equilibrium with atmospheric oxygen found the oxidation of pyrite released sulfate and Fe(II)⁶⁰. Elevated levels of Fe, presumably Fe(II), is a widespread observation in the FPW of numerous formations in addition to the Duvernay Formation, including the Marcellus Formation (0.3-747 mg/L)^{20,21,61}, Barnett

Formation (50-300 ppm)⁷¹, Bakken Formation (0.7-96 ppm)⁶² and Bowland Formation (36.6-137 mg/L)⁶⁴. The aeration of S3 resulted in a 75.6% decrease in aqueous Fe(II), and in terms of color, from transparent yellow to turbid orange (Figure SI.2). Collectively, the decrease in aqueous Fe(II), change in color and increase in turbidity are consistent with the precipitation Fe(III) oxyhydroxides, such as ferrihydrite (Fe(OH)₃), as has been previously hypothesized to account for losses of aqueous Fe during the handling of Marcellus FPW by Phan et al.³⁸ and Tasker et al.⁶⁵.

3.2 XRD Analysis

Both samples of drill cuttings from well 3 were found to contain quartz, calcite, muscovite, and aragonite (Figure SI.3). Sample A was found to contain sanidine, while sample B had kaolinite. The results of the bulk analysis are in generally in agreement with the literature for the composition of Duvernay Formation. The shales and argillites of the Duvernay have been shown to be primarily composed of quartz, mica, feldspar, plagioclase, calcite, and illite/smectite with less amounts of kaolinite^{47,48}. There due to the heterogeneity within the formation it is not unsurprising that pyrite and barite might not found in the two samples which can be locally common^{48,66}.

3.3 Solids Analysis

The chemical composition of the solids for each sample were dominated by Fe and Si, with lesser amounts of S, Ca, Sr, and Ba (Figure 1 and SI.4 for mg/kg). Trace amounts (less than 100 mM) of Al, K, Mg, P, Mn, and Zn were detected, however, not in every sample (Table SI.1). The largest variations between samples was their ratios of Si to Fe, not their elemental composition. S1 was predominately Fe-rich, with the next most abundant element being Si (3351 mM/kg); S,

Ba, Ca, and Sr were the only other elements greater than 99 mM/kg. In contrast, S2 had an excess of Si to Fe 5842 to 1630 mM/kg respectively. Additionally, S2 had the highest amounts of S (778 mM/kg), and Sr (717 mM/kg). S3 also had a Si:Fe ratio greater than 1 (1.34) and had the highest ratios of Ca and Ba, 0.21 and 0.16, respectively. The Sr+Ba:S molar ratio for all samples was approximately 1 and 0.89, 0.98, and 0.94 for S1, S2, and S3, respectively. In contrast, the relative abundances of Ba and Sr do vary: S1 and S3 have a relative excess of Ba to Sr, 1.37 and 1.42, while S2 contained a low Ba to Sr ratio, 0.07.

Aerating S3 (S3_Ox) resulted in the decline of the relative ratio of Si/Fe from an excess of Si to an excess of Fe ($\text{Si/Fe} = 0.41$). The ratios of Si, Ba, Ca, and Sr to Fe also declined. Aeration was effective in the removal of dissolved Fe(II) and the concomitant generation of Fe(III) precipitates. The Ba/S ratio between samples S3 and S3_Ox were similar at 0.55 and 0.59, respectively, while the ratio of Sr/S showed a Sr enrichment in S3_Ox (0.61) compared to S3 (0.39). The removal of Sr during aeration is also evident in the relative abundance of Ba/Sr which shifted from 1.41 (excess Ba) to 0.98. The removal of Sr from solution during aeration suggests its adsorption or incorporation during the precipitation of the Fe(III) oxyhydroxides. The incorporation of Sr into iron oxides has previously been observed during ferrihydrite ripening to goethite⁶⁷.

3.4 Morphological and Chemical Characterization

The backscatter SEM images (Figures 2 A, C, E, and G) show the solids had two particle morphologies: (1) globular neoformed aggregates, and (2) stellated clusters. For both particle types, the strong C signals observed were attributed to the carbon coating used to prepare the samples and the carbon-based tape used to affix samples to the aluminum tabs, and the strong O

signal primarily to O associated with the mineral oxides that comprise the solids. We cannot exclude the possibility that a portion of the C and O signal was related to organic compounds associated with the sample, however, with the carbon tape it is impossible to quantify what portion that may be. Investigating whether there is significant insoluble organic carbon associated with the FPW solids will need to be investigated in the future. For the purposes of this study, C and O have been excluded from the discussion that follows. The EDS spectrum (gray bars) of S1's globular, neoformed aggregates have an approximate composition in molar percent of: Si (2.19%) and Fe (5.13%) (Figure 2 B). The neoformed aggregates in S2 and S3 showed similar elemental profiles (Figure 2 D, H). However, for S3_Ox, an increase in the relative molar percent of Fe was observed (Figure 2F and H). While the ratio of Fe to Si varied between samples and EDS spots, neither element was found independent of the other. These observations suggest that the neoformed aggregates are discrete Fe/Si phases, representative of a silica-enriched Fe(III) oxyhydroxide.

Representative EDS spectra targeting the stellated clusters in S1 (Figure 2 B) show that they are composed of S (4.19%), Sr (1.54%), Ba (3.02%), Si (1.54%), and Fe (2.78%), with a close association between S, Ba and Sr. stellated clusters from S2, S3, and S3_Ox exhibited similar elemental profiles (Figures 2 D, F, and H). This correlation was not observed in the neoformed aggregates. Fe and Si were not observed in every spectrum with S, Ba, and Sr. We attributed the low presence of Fe and Si in the EDS spectra as an artifact of the large EDS spot size, which resulted in the EDS beam also contacting part of the neoformed aggregates silica-enriched Fe(III) oxyhydroxide. The consistent elemental profile of stellated clusters indicates that they are singular phase composed of Sr, Ba, and S, with a Sr+Ba:S molar ratio of approximately 1. This is consistent with a sulfate mineral such as barite or celestine.

Across all three samples, the neoformed aggregates of the untreated samples showed a similar spherical particle morphology and size (~200 nm) (Figure 3 A, B, and C). Aerating S3 generated additional neoformed aggregates of a similar size and morphology to those found in the untreated samples (Figure 3 D). A comparison of S3 and S3_Ox revealed that S3 had plates of granular aggregates composed of 200 nm spherical particles with a few aggregates associated with the surfaces, while S3_Ox has numerous colloidal aggregates on the surfaces (Figure 3 A and B).

HRTEM with EDS and SAED was further used to probe the composition and mineralogy of the Fe/Si phase. HRTEM images of S1 reveal a lack of order amongst the neoformed aggregates, with no visible edge steps (Figure 4 A and B). The elemental composition was dominated by Fe and Si (Figure 4 D). The SAED pattern generated from the Fe/Si aggregates (Figure 4 C) showed no apparent diffraction pattern, indicating a lack of crystallinity consistent with an amorphous silica enriched Fe(III) oxyhydroxide phase. STEM elemental maps of the solids from sample 1 show a strong association between Fe, Si and O (Figure SI.5 A, B, and C). The Si appears to have a higher abundance at the core of the particle with the Fe aggregating on the Si core. The elemental map of the Sr+Ba:S phase shows that a higher concentration of S compared to Sr or Ba and that all three elements are concentrated in the particle (Figure SI.6 A, B, C, and D)

3.5 Modeled Saturation Indices

The saturation indices of each sample were calculated as a function of temperature, from 10 to 120° C. This represents the approximate range of temperatures that FPW would encounter as it returns from the elevated subsurface temperatures, approximately 115° C for the Duvernay

Formation⁶⁸, and equilibrates at the surface. The thermodynamic modeling was performed in PHREEQC⁶⁹ utilizing the Pitzer database due to the high ionic strength of the FPW samples 4.11, 3.24 and 3.31 M for S1, S2, and S3, respectively. The Pitzer database included barite (BaSO₄), celestine (SrSO₄), quartz (SiO₂), and amorphous silica (SiO_{2(am)}). To model the SI, the measured concentrations from S1, S2, and S3 of all elements found to be greater than 100 ppm (Na, Cl, Ca, K, Sr, Br, and Mg) and Fe, S, Ba, and Si were utilized, with the pH set at that measured for each respective sample. For the purpose of this model all S from the total dissolved S measurement was assumed to be sulfate (SO₄²⁻) during modeling. S speciation in flowback is known to include thiosulfate and hydrogen sulfide, however, they have been found to be relatively minor components totaling less than 10% the sulfate concentration⁷⁰. To begin, the sensitivity of the saturation indices to changes in pH was examined the models were run as pH sweeps from 3-10. The saturation indices for barite and celestine were found to not be sensitive to pH across the pH range examined (Figure SI.7 A and B), while the saturation indices of silica was found to decrease exponentially above pH 8, well above the pH of the FPW samples examined (Figure SI.8). Additionally, the models were examined for to determine whether the exsolution of CO₂ may have occurred during the cooling process, which could have influenced changes in FPW pH, however, across the temperature range examined the saturation indices for CO₂ was well below 0 (Figure SI.9).

S1, S2, and S3 were found to be supersaturated with respect to barite at room temperature (20°C). The saturation indices show a distinct trend of increasing with decreasing temperature, which indicates that it is more thermodynamically favorable to form a solid phase as the solution cools (Figure 5 A). S3 had the highest equilibrium temperature, approximately 90°C, which may be attributed to its being the freshest sample and the process of precipitation being kinetically

slow. In contrast, all three samples were found to be undersaturated with respect to celestine with saturation indices ranging from -0.28 to -0.66 across the entire temperature range examined (Figure 5 B). As the models were performed using elemental analysis collected on solutions that had been fully cooled, this does not mean that the solution was not previously supersaturated with respect to celestine. It is more plausible that the Sr concentration was initially drawn down during the cooling by the precipitation of celestine. The continued precipitation of barite after the celestine reached equilibrium likely drew down the sulfate concentration and potentially the Sr concentration through incorporation to reflect the measured undersaturated concentrations. Interestingly, S2 had the lowest saturation indices and the lowest Ba/Sr ratio in the sediment (0.070).

While Si was found in solids of all three samples, Si was only above the detection limit in the aqueous phase of S1. For S1 we modelled the saturation indices for this sample with respect to the two silicate minerals quartz and amorphous silica. At room temperature, S1 was supersaturated with respect to quartz but not $\text{SiO}_{2(\text{am})}$. S1 was supersaturated with respect to quartz below 60°C; in contrast the lowest saturation indices for $\text{SiO}_{2(\text{am})}$ was -0.67 (Figure 6). Furthermore, we modeled each sample in equilibrium with respect to either barite and celestine or quartz and $\text{SiO}_{2(\text{am})}$ to determine how the measured Si, Ba, Sr, and sulfate concentrations compared to the modeled equilibrium concentrations. Regarding the silicate minerals, S1 had an excess of Si with respect to quartz below 80°C, respectively. In contrast, S1 was below the modeled Si equilibrium concentration with respect $\text{SiO}_{2(\text{am})}$ across the entire temperature range, but by less than 1 mM when the temperature was below 30 °C (Figure SI.11). Even if we assume samples S2 and S3 had no measurable Si in solution, they too are still only below the equilibrium

concentration of Si by less than one mM for quartz across the entire temperature range, and by less than one mM when the temperature is at or below 20 °C for $\text{SiO}_{2(\text{am})}$.

For S1, the system was found to be supersaturated with respect to sulfate across the modeled temperature range and to have an excess of Ba when the temperature was below 50°C. Across the examined temperature range, Sr was below the equilibrium concentration by 2.26-3.04 mM (Figure SI.10 A). Similarly, S3 had an excess of sulfate and Ba across the entire temperature range and Sr was below the equilibrium concentration by 2.62 - 3.59 mM (Figure SI.10 C). In contrast, S2 was below the equilibrium concentrations of sulfate and Sr across the entire temperature range, by 56.4 and 20.1 mM respectively, while below 70° C there was an excess of Ba (Figure SI.10 B).

3.6 Multi-basin Comparison

Publicly available FPW chemistry data for the Fayetteville (4 samples)⁷⁰, Marcellus (day 14 flowback median from 7 wells, average of 95 well, 2 composite samples of days)^{20,21,34}, Bakken (median of 4 wells from day 10-12)⁶², Barnett (median from day 10-12 from 4 wells)⁶³ and Denver-Julesburg (DJ) Formations (4 wells)⁷³ were modeled for using the same PHREEQC model developed for the Duvernay Formation (Full modeling parameters are shown in Table saturation indices 2). While each basin is expected to have heterogeneity, these models offer a first pass determine how similar the FPW solids are between shale basins and how widely applicable treatment options would be. In the case of absent pH data for the Fayetteville and Marcellus, the pH was assumed to be 7 as the models only showed a pH dependence above pH 8.

For barite, below 90⁰ C the precipitation was found to be favorable (saturation indices greater than 1) for FPW from the Marcellus, Bakken, Barnett and DJ formations for all sample

where the sulfate concentration was reported (Figure 7 A). Below 30⁰ C this also included the Duvernay. The Fayetteville was the only formation for which the precipitation of barite was not thermodynamically favorable across the temperature range. In contrast the precipitation of celestine was favorable for 3 out of the 4 Marcellus samples across the entire temperature range examined (Figure 7 B). For all other basins, the formation of celestine was not favorable at any temperature. However, as observed in this study for the Duvernay, this does not preclude the possibility of Sr incorporation into barite or the formation of a solid solution of Sr/Ba(SO₄). For all basins save the Fayetteville the saturation indices for celestine was greater than -1, meaning it is close to being in equilibrium with celestine.

Saturation indices for quartz and SiO_{2(am)} was only modeled, in addition to the Duvernay Formation, for Fayetteville and DJ as dissolved silica data was not available for the Bakken, Marcellus and Barnett. SiO_{2(am)} was found to have a saturation indices greater than 0 only for 1 out of 5 of the Fayetteville FPW samples (Figure 8 A). In contrast the formation of quartz was found to be favorable in all three basins with dissolved Si data below 50⁰ C (Figure 8 B). Additionally, for the Marcellus while the absence of dissolved silica data precluded the modeling of saturation indices silica has been identified through SEM EDS analysis of solids fouling filters used for Marcellus FPW³⁴. This indicates the absence of dissolved silica data or when it is found to be below the detection limit would not mean that the formation of quartz would not be favorable.

Additionally, appreciable concentrations dissolved Fe were reported in each of the basins Fayetteville (1-13 ppm)⁷¹, Marcellus (40.8-747 ppm)^{20,21,34}, Bakken (0.7-96 ppm)⁶², Barnett (12.1-93.8 ppm)⁷² and DJ (2.71-19)⁷³. This indicates that the precipitation of insoluble Fe(III)

oxyhydroxides is likely across more than the Duvernay and Marcellus Formations where it has already been observed^{38,65}.

3.7 Mechanisms of Formation

The amorphous Fe/Si phase likely formed through a two-step process. First, the FPW returned to the surface from the target formation with an elevated temperature (~115°C for the Duvernay⁶⁸, 82°C for the Fayetteville⁷⁴, 104 °C for the Marcellus⁷⁵, 71-116 °C for the Bakken⁷⁶, 93 °C for the Barnett⁷⁴, and 116 °C for the DJ Formation⁷⁷ and enriched in dissolved Si relative to surface temperatures^{54,55}. As the FPW cooled, Si became increasingly supersaturated with respect to amorphous silica. Second, with the increasing oxygen solubility and diffusion associated with cooling, the dissolved Fe(II) oxidized to Fe(III), and through subsequent hydrolysis formed insoluble Fe(III) oxyhydroxides. The Fe(II), and at least a portion of the sulfate, was probably derived from the oxidation of pyrite (FeS₂) by oxygenated fracturing fluid. In this process sulfide in pyrite in the formation oxidized to sulfate, consuming the oxygen in the fracturing fluid releasing sulfate and Fe(II) into solution⁶⁰. The subsurface conditions rapidly return to anoxic after the oxygen is consumed through sulfide oxidation, which prevents the Fe(II) from also oxidizing to Fe(III). The Fe(III) oxyhydroxides are always closely associated with amorphous silica, an unsurprising observation given that Fe(III) oxyhydroxides have a high sorption capacity for dissolved silica^{78,79}. However, in our study the evidence points towards the adsorption and templating of Fe(III) oxyhydroxides onto amorphous silica to be the process by which this phase formed. Additionally, the diffusion of oxygen may be limited by thin surface oil films on the FPW, as were observed in our samples. Nonetheless, the residual Fe(II) can be oxidized through treatments, such as aeration (see S3_Ox).

The mechanism(s) by which the FPW solids form similarly sized Fe/Si particles (~200 nm diameter) could be related to several factors including, the rate of cooling and/or Fe(II) oxidation, high ionic strength, or presence of organic matter (OM). OM is known to alter Fe(II) oxidation rates, control the final mineral formed during mineralization, and in tandem with Si, prevent the ripening of low order iron-oxide species into crystalline forms^{80, 81}. The incorporation and adsorption of OM by iron-oxides can alter their surface charge preventing aggregation or agglomeration and enhancing their incorporation of contaminants^{82,83}.

The second solid phase, a mixed Sr/Ba sulfate, is representative of a barite-celestine solid solution. BaSO₄ and SrSO₄ have been found in Marcellus FPW⁸⁴ and their solubilities are temperature dependent^{85,86}. The Sr/Ba-SO₄ phase likely formed as a function of the FPW cooling from the subsurface to surface temperatures and creating supersaturated conditions that drive their precipitation. Its precipitation is likely rapid, as barite scale formation increases with increasing ionic strength with Na initiating the growth of new step rows; the latter is the rate limiting step in low ionic strength solutions⁸⁷.

3.8 Environmental Implications

The characterization of FPW solids will enhance the development of new FPW treatment options for reuse, contaminant removal, and transportation risk reductions. To date, the solids have been observed to account for approximately 50% of FPW's PAH load^{1,45} and approximately 50% of their total toxicity as measured by LC₅₀ and EROD^{1,46}. Other organic contaminants may also be associated with the solids as only targeted analysis of PAHs have thus far been conducted. As Fe(III) oxyhydroxides were the dominant solid phase, and they are known to adsorb organic contaminants such as PAHs⁸⁸, we hypothesize that majority of PAHs

associated with the solids are sorbed to the Fe(III) oxyhydroxides. Furthermore, the fact that the aeration of the FPW generated additional approximately 200 nm diameter Fe/Si particles opposed to resulting in the growth of the previously existing particles is important. These freshly generated Fe/Si particles represent a large increase the particle reactive surface area in the FPW per litre and should enhance the ability of the solids to remove contaminants. Additionally, during simulated hydraulic fracturing experiments with shales containing pyrite and simulated hydraulic fracturing fluids containing dissolved oxygen, Xiong et al.⁴⁹ observed the generation of hydroxyl radicals and degradation of one HFF chemical, polyacrylamide. They hypothesized that the Fe(II) released by the pyrite in the presence of dissolved oxygen resulted in a free radical chain scission mechanism. Given the wide spread occurrence of presumably Fe(II) in FPW the aeration of FPW to promote the formation of Fe(III) oxyhydroxides by oxidizing residual Fe(II) has the potential to be a widespread treatment technique to remove additional organic contaminants, adsorb or incorporate heavy metals, and reduce the aqueous toxicity of FPW.

While NORMs have not appreciably been found in Duvernay Formation²⁷ FPW, they are a concern in other formations, such as the Marcellus Formation^{25,26}. Ba and Sr sulfates are known to incorporate NORMs such as radium during their formation^{35,89}. Therefore, NORMs and their associated risks could be concentrated in the solid phase. Adding sulfate to FPW has been proposed as a treatment to remove Sr and Ba from FPW³⁵. Thus, understanding the sources of Ba⁵⁶ and removing it from FPW could promote the reuse of FPW by reducing the risk of barite scales⁹⁰. The disposal of these solids, however, would need to account for any NORMs concentrated during treatment.

Additional work will be required to characterize the solids from other basin and understand the mechanisms by which heavy metals, NORMs, and organic contaminants, such as

PAHs^{1,45,46}, adsorb and desorb from FPW associated solids. This work could be important for remediating FPW spills. Furthermore, treatments that generate iron oxides could remove additional contaminants, reduce the environmental risks associated with FPW, and prevent their formation during the recycling of FPW. These insights will promote the further development of treatment technologies for the reuse of FPW.

Acknowledgements

The research presented in this manuscript was funded by Natural Sciences and Engineering Research Council of Canada (NSERC) Collaborative Research and Development (CRD) grant CRDPJ 469308-14 and support from the Encana Corporation to D.S.A., G.G.G and J.W.M. Special thanks to Dr. Gerein at the SEM Laboratory at the University of Alberta and Dr. Mukasyan at the Integrated Imaging Facility at the University of Notre Dame for assistance in sample imaging, Dr. Jeremy Fein at the University of Notre Dame for facilitating access, and Johanna Weston at Newcastle University for manuscript support. Additionally, we would like to thank the three reviewers for their challenging and helpful suggestions, which aided in the significant improvement of this manuscript.

References

- (1) Y. He, S.L. Flynn, E.J. Folkerts, Y. Zhang, D. Ruan, D.S. Alessi, J.W. Martin, and G.G. Goss, Chemical and toxicological characterization of hydraulic fracturing flowback and produced waters, *Water Res.*, 2017a, **114**, 78-87.

- 530 (2) G.P. Macey, R. Breech, M. Chernaik, C. Cox, D. Larson, D. Thomas, and D.O.
531 Carpenter, Air concentrations of volatile compounds near oil and gas production: a community-
532 based exploratory study, *Enviro. Health*, 2014, **13**.
- 533 (3) R. Davies, G. Foulger, A. Bindley, and P. Styles, Induced seismicity and hydraulic
534 fracturing for the recovery of hydrocarbons, *Mar. and Pet. Geol.*, 2013, **45**, 171-185.
- 535 (4) K.M Keranen, M. Weingarten, G.A. Abers, B.A. Bekins, and S. Ge, Sharp increase in
536 central Oklahoma seismicity since 2008 induced by massive wastewater injection, *Science*, 2014,
537 **385**, 448-451.
- 538 (5) D.W. Eaton, and A.B. Mahani, Focal Mechanisms of Some Inferred Induced Earthquakes
539 in Alberta, Canada, *Seismological Research Letters*, 2015, **86**, 1078–1085.
- 540 (6) S. Goodwin, K. Carlson, K. Knox, C. Douglas, and L. Rein, Water intensity assessment
541 of shale gas resources in the Wattenberg Field in Northeastern Colorado, *Environ. Sci. Technol.*,
542 2014, **48**, 5991-5995.
- 543 (7) A. Kondash, and A. Vengosh, Water footprint of hydraulic fracturing, *Environ. Sci.*
544 *Technol. Lett.*, 2015, **2**, 276-20.
- 545 (8) D.S. Alessi, A. Zolfaghari, S. Kletke, J. Gehman, D.M. Allen, and G.G. Goss,
546 Comparative analysis of hydraulic fracturing wastewater practices in unconventional shale
547 development: Water sourcing, treatment and disposal practices, *Canadian Water Resources*
548 *Journal*, 2017, **42**, 105-121.
- 549 (9) Vidic RD, Brantley SL, Vandenbossche JM, and Abad JD (2013) Impact of shale gas
550 development on regional water quality, *Science*, **340**, 826-835.

551 (10) G.T. Llewellyn, F. Dorman, J.L. Westland, D. Yoxtheimer, P. Grieve, T. Sowers, E.H.
552 Fulmer, and S.L. Brantley, Evaluating a groundwater supply contamination incident attributed to
553 Marcellus Shale gas development, *Proc. Natl. Acad. Sci. U.S.A.*, 2015, **112**, 6325-6330.

554 (11) J.B. Jacquet, Review of risks to communities from shale energy development, *Environ.*
555 *Sci. Technol.*, 2014, **48**, 8321-8333.

556 (12) C.D. Kassotis, L.R. Iwanowicz, D.M. Akob, I.M. Cozzarelli, A.C. Mumford, W.H.
557 Orem, and S.C. Nagel SC, Endocrine disrupting activities of surface water associated with a
558 West Virginia oil and gas industry wastewater disposal site, *Sci. Total Environ.*, 2016, **557-558**,
559 901-910.

560 (13) E.E. Yost, J. Stanek, R.S. Dewoskin, and L.D. Burgoon, Overview of chronic oral
561 toxicity values for chemicals present in hydraulic fracturing fluids, flowback, and produced
562 waters, *Environ. Sci. Technol.*, 2016, **50**, 478-4797.

563 (14) N.R. Warner, R.B. Jackson, T.H. Darrah, S.G. Osborn, A. Down, K. Zhao, A. White, and
564 A. Vengosh, Geochemical evidence for possible natural migration of Marcellus Formation brine
565 to shallow aquifers in Pennsylvania, *Proc. Natl. Acad. Sci. U.S.A.*, 2012, **109**, 11961-11966.

566 (15) D.C. DiGuilio, and R.B. Jackson, Impact to Underground Sources of Drinking Water and
567 Domestic Wells from Production Well Stimulation and Completion Practices in the Pavilion,
568 Wyoming, Field, *Environ. Sci. Technol.*, 2016, **50**, 4524-4536.

569 (16) J.S. Harkness, T.H. Darrah, N.R. Warner, C.J. Whyte, M.T. Moore, R. Millot, W.
570 Kloppman, R.B. Jackson, and A. Vengosh, The geochemistry of naturally occurring methane and

571 saline groundwater in an area of unconventional shale gas development, *Geochim. Cosmochim.*
572 *Acta*, 2017, **208**, 302-334.

573 (17) R.B. Jackson, A. Vengosh, W.J. Carey, R.J. Davies, T.H. Darrah, F. O’Sullivan, and G.
574 Petron, The environmental costs and benefits of fracking, *Annual Reviews of the Environment*
575 *and Resources*, 2014, **39**, 327-362.

576 (18) L.A. Patterson, K.E. Konschnik, H. Wiseman, J. Fargione, K.O. Maloney, J. Kiesecker,
577 J.P. Nicot, S.B. Mordo, S. Entrekin, A. Trainor, and J.E. Saiers, Unconventional oil and gas
578 spills: risks, mitigation priorities, and state reporting requirements, *Environ. Sci. Technol.*, 2017,
579 **51**, 2563-2573.

580 (19) R.S. Balaba, and R.B. Smart, Total arsenic and selenium analysis in Marcellus shale,
581 high-salinity water, and hydrofracture flowback wastewater, *Chemosphere*, 2012, **89**, 1437-1442.

582 E. Barbot, N.S. Vidic, K.B. Gregory, and R.D. Vidic, Spatial and temporal correlation of water
583 quality parameters of produced waters from Devonian age shale following hydraulic fracturing,
584 *Environ. Sci. Technol.*, 2013, **47**, 2562-2569.

585 (20) E. Barbot, N.S. Vidic, K.B. Gregory, and R.D. Vidic, Spatial and temporal correlation of
586 water quality parameters of produced waters from Devonian age shale following hydraulic
587 fracturing, *Environ. Sci. Technol.*, 2013, **47**, 2562-2569.

588 (21) L.O. Haluszczak, A.W. Rose, and L.R. Kump, Geochemical evaluation of flowback brine
589 from Marcellus gas wells in Pennsylvania, USA, *Appl. Geochem.*, 2013, **28**, 55-61.

- 590 (22) Y. Lester, I. Ferrer, E.M. Thurman, K.A. Sitterly, J.A. Korak, G. Aiken, and K.G.
591 Linden, Characterization of hydraulic fracturing flowback water in Colorado: implications for
592 water treatment, *Sci. Total Environ.*, 2015, **512-513**, 637-644.
- 593 (23) S. Kim, P.O. Ozbek, A. Dhanasekar, A. Prior, and K. Carlson, Temporal analysis of
594 flowback and produced water composition from shale oil and gas operations: impact of frac fluid
595 characteristics, *J. Pet. Sci. Eng.*, 2016, **147**, 202-210.
- 596 (24) A. Zolfaghari, H. Dehghanpour, M. Noel, and D. Bearinger, Laboratory and field analysis
597 of flowback water from gas shales, *Journal of Unconventional Oil and Gas Resources*, **14**, 2016,
598 113-127.
- 599 (25) S. Almond, S.A. Clancy, R.J. Davies, and F. Worrall, The flux of radionuclides in
600 flowback fluid from shale gas exploitation, *Environ. Sci. Pollut. Res.*, 2014, **21**, 12316-12324.
- 601 (26) A.W. Nelson, D. May, A.W. Knight, E.S. Eitheim, M. Mehroff, R. Shannon, R. Litman,
602 and M.K. Schultz, Matrix complications in the determination of radium levels in hydraulic
603 fracturing flowback water from Marcellus shale, *Environ. Sci. Technol. Lett.*, 2014, **1**, 204-208.
- 604 (27) K. Hoelzer, A.J. Sumner, O. Karatum, R.K. Nelson, B.D. Drollette, M.P. O'Conner, E.L.
605 D'Ambro, G.J. Getzinger, P.L. Ferguson, C.M. Reddy, M. Elsner, and D.L. Plata, Indications of
606 transformations products from hydraulic fracturing additives in shale-gas wastewater, *Environ.*
607 *Sci. Technol.*, 2016, **50**, 8036-8048.
- 608 (28) D.M. Akob, I.M. Cozzarelli, D.S. Dunlap, E.L. Rowen, and M.M. Lorah, Organic and
609 inorganic composition and microbiology of produced waters from Pennsylvania shale gas wells,
610 *Appl. Geochem.*, 2015, **60**, 116-125.

- 611 (29) K. Oetjen, and L. Thomas, Volatile and semi-volatile organic compound patterns in
612 flowback waters from fracturing sites within the Marcellus Shale, *Environ. Earth Sci.*, 2016, **75**,
613 1043.
- 614 (30) E.M. Thurman, I. Ferrer, J. Blotevogel, and T. Borch, Analysis of hydraulic fracturing
615 flowback and produced waters using accurate mass: identification of ethoxylated surfactants,
616 *Anal. Chem.*, 2014, **86**, 9635-9661. J.S. Rosenblum, K.A. Sitterley, E.M. Thurman, I. Ferrer, and
- 617 (31) K.G. Linden, Hydraulic fracturing wastewater treatment by coagulation-adsorption for
618 removal of organic compounds and turbidity, *J. Environ. Chem. Eng.*, 2016, **4**, 1978-1984.
- 619 (32) E.M. Thurman, I. Ferrer, J. Rosenblum, K. Linden, and J.N. Ryan, Identification of
620 polypropylene glycols and polyethylene glycol carboxylates in flowback and produced water
621 from hydraulic fracturing, *J. Hazard. Mater.*, 2017, **323**, 11-17.
- 622 (33) I. Ferrer, and E.M. Thurman, Analysis of hydraulic fracturing additives by LC/Q-TOF-
623 MS, *Anal. Bioanal. Chem.*, 2015, **407**, 6417-6428.
- 624 (34) C. He, X. Wang, W. Liu, E. Barbot, and R.D. Vidic, Microfiltration in the recycling of
625 Marcellus Shale flowback water: solids removal and potential fouling of polymeric
626 microfiltration membranes, *J. Membr. Sci.*, 2014c, **462**, 88-95.
- 627 (35) C. He, T. Zhang, and R.D. Vidic, Co-treatment of abandon mine drainage and Marcellus
628 Shale flowback waters for using in hydraulic fracturing, *Water Res.*, 2016, **104**, 425-431.
- 629 (36) B. Xiong, A.L. Zydney, and M. Kumar, Fouling of microfiltration membranes by
630 flowback and produced waters from the Marcellus shale gas play, *Water Res.*, 2016, **99**, 162-170.

631 (37) G. Li, B. Bai, and K.H. Carlson, Characterization of solids in produced water from wells
632 fracturing with recycled and fresh water, *Journal of Petroleum Science and Engineering*, 2016,
633 **114**, 91-98.

634 (38) T.T. Phan, J.A. Hakala, and D.J. Bain, Influence of colloids on metal concentrations and
635 radiogenic strontium isotopes in groundwater and oil and gas-produced waters, *Appl. Geochem.*,
636 2018, **95**, 85-96.

637 (39) M.C. Graham, I.W. Oliver, A.B. Mackenzie, R.M. Ellam, and J.G. Farmer, Mechanisms
638 controlling lateral and vertical porewater migration of depleted uranium (DU) at two UK
639 weapons testing sites, *Sci. Tot. Environ.*, 2011, **409**, 1854-1866.

640 (40) Y. Wang, M. Frutschi, E. Suvorova, V. Phommavanh, M. Descostes, A.A.A. Osman, G.
641 Geipel, and R. Bernier-Latmani, Mobile uranium (IV)-bearing colloids in a mining impacted
642 wetland, *Nat. Commun.*, 2013, **4**.

643 (41) A.B. Kersting, D.W. Efur, D.L. Finnegan, D.J. Rokop, D.K. Smith, and J.L. Thompson,
644 Migration of plutonium in ground water at the Nevada Test Site, *Nature*, 1999, **397**, 56-59.

645 (42) A.P. Novikov, S.N. Kalmykov, S. Utsunomiya, R.C. Ewing, F. Horreard, A. Merkulov,
646 S.B. Clark, V.V. Tkachev, and B.F. Myasoedov, Colloid transport of plutonium in the far-field
647 of Mayak production association, Russia, *Science*, 2006, **314**, 638-641.

648 (43) D.A. Backhus, J.N. Ryan, D.M. Groher, J.K. MacFarlane, and P.M. Gschwend, (1993)
649 Sampling colloids and colloid-associated contaminants in ground water, *Groundwater*, 1993, **31**,
650 466-479.

- 651 (44) A.A. Mackay, and P.M. Gschwend, Enhanced concentrations of PAHs in groundwater at
652 a coal tar site, *Environ. Sci. Technol.*, 2001, **35**, 1320-1328.
- 653 (45) Y. He, E.J. Folkerts, Y. Zhang, J.W. Martin, D.S. Alessi, and G.G. Goss, Effects on
654 biotransformation, oxidative stress, and endocrine disruption in rainbow trout (*Oncorhynchus*
655 *mykiss*) exposed to hydraulic fracturing flowback and produced waters, *Environ. Sci. Technol.*,
656 2017b, **51**, 940-947.
- 657 (46) Y. He, C. Sun, E.J. Folkerts, J.W. Martin, and G.G. Goss, Developmental toxicity of the
658 organic fraction from hydraulically fractured flowback and produced waters to early life stages
659 of zebrafish (*Danio rerio*), *Environ. Sci. Technol.*, 2018, **52**, 3820-3830.
- 660 (47) S.D.A. Anderson, C. D. Rokosh, J.G. Pawlowicz, H. Berhane and A. P. Beaton, 2010,
661 Mineralogy, permeametry, mercury porosimetry, pycnometry and scanning electron microscope
662 imaging of Duvernay and Muskwa Formations in Alberta: Shale Gas Data Release: ERCB/AGS
663 Open File 830 Report, https://ags.aer.ca/document/OFR/OFR_2010_02.pdf (Accessed
664 November 2018).
- 665 (48) M.R. Yassin, M. Begum, and H. Dehghanpour, Organic shale wettability and its
666 relationship to other petrophysical properties: A Duvernay case study. *International Journal of*
667 *Coal Geology*, 2017, **169**, 74-91.
- 668 (49) B. Xiong, Z. Miller, S. Roman-White, T. Tasker, B. Farina, B. Piechowicz, W.D. Burgos,
669 P. Joshi, L. Zhu, C.A. Gorski, A.L. Zydney, Chemical Degradation of Polyacrylamide during
670 Hydraulic Fracturing, *Environ. Sci. Technol.*, 2017, **52**, 327-36.
- 671 (50) T.A. Blewett, P.L.M Delompre, Y. He, E.J. Folkerts, S.L. Flynn, D.S. Alessi, and G.G.
672 Goss, Sublethal and reproductive effects of acute and chronic exposure to flowback and

673 produced water from hydraulic fracturing on the water flea *Daphnia magna*, *Environ. Sci.*
674 *Technol.*, 2017, **51**, 3032-3039.

675 (51) GBC Scientific Equipment: The determination of aluminum, iron and silicon in rock
676 samples, http://www.gbcscientific.com/appnotes/AA_app_note_001.pdf, (accessed May 2016)

677 (52) K. von Gunten, M.S. Alam, M. Hubmann, Y.S. Ok, K.O. Konhauser, and D.S. Alessi,
678 Modified sequential extraction for biochar and petroleum coke: Metal release potential and its
679 environmental implications, *Bioresource Technology*, 2017, **236**, 106-110.

680 (53) K. Porsch, and A. Kappler, Fe(II) oxidation by molecular O₂ during HCl extraction,
681 *Environ. Chem.*, 2011, **8**, 190-197.

682 (54) J.V. Walther, and H.C. Helgeson, Calculation of the thermodynamic properties of
683 aqueous silica and the solubility of quartz and its polymorphs at high pressure and temperature,
684 *Amer. J. Sci.*, 1977, **277**, 241-251.

685 (55) C.T. Chen, and W.L. Marshall, Amorphous silica solubilities IV. Behavior in pure water
686 and aqueous sodium chloride, magnesium chloride, sodium sulfate, magnesium chloride, and
687 magnesium sulfate solutions up to 350 C, *Geochim. Cosmochim. Acta*, 1982, **46**, 279-297.

688 (56) D. Renock, J.D. Landis, and M. Sharma, Reductive weathering of black shale and release
689 of barium during hydraulic fracturing, *Appl. Geochem.*, 2016, **65**, 73-86.

690 (57) P. Bennett and D.I. Siegel, Increasing solubility of quartz in water due to complexing by
691 organic compounds, *Nature*, 1987, **326**, 684-686)

692 (58) P. Bennett, Quartz dissolution in organic-rich aqueous systems, *Geochim. Cosmochim.*
693 *Acta*, 1991, **55**, 1781-1797.

694 (59) A.D. Jew, M.K. Dustin, A.L. Harrison, C.M.J. Wong, D.L. Thomas, K. Maher, G.E.
695 Brown, and J.R. Bargar, Impact of organics and carbonates on the oxidation and precipitation of
696 iron during hydraulic fracturing of shale, *Energy and Fuel*, 2017, **31**, 3643-3658.

697 (60) M. Xu, M. Binazadeh, A. Zolfaghari, and H. Dehghanpour, Effects of dissolved oxygen
698 on water imbibition in gas shales, *Energy and Fuels*, 2018, **32**, 4695-4704.

699 (61) N. Abualfaraj, P.L. Gurian, and M.S. Olson, Characterization of Marcellus Shale
700 Flowback Water, *Environ. Eng. Sci.*, 2014, **31**, 514-524.

701 (62) N. Shrestha, G. Chilkoor, J. Wilder, V. Gadhamshetty, and J.J. Stone, Potential water
702 resource impacts of hydraulic fracturing from unconventional oil production in the Bakken
703 Shale, *Water Res.*, 2017, **108**, 1-24.

704 (63) A. Shramko, T. Palmgren, D. Gallo, and R. Dicit, Analytical Characterization of
705 flowback waters in the field, 16th Annual Petroleum and Biofuels Environmental Conference
706 (IPEC), Houston, November 3-5, 2009.

707 (64) Environment Agency Report: Shale gas north west—monitoring of flow back water,
708 [http://webarchive.nationalarchives.gov.uk/20140328145127/http://www.environment-](http://webarchive.nationalarchives.gov.uk/20140328145127/http://www.environment-agency.gov.uk/static/documents/Business/6th_Dec_-_Shale_gas_-_North_West_-_Monitoring_of_flowback_water_-_update_(3).pdf)
709 [agency.gov.uk/static/documents/Business/6th_Dec_-_Shale_gas_-_North_West_-](http://webarchive.nationalarchives.gov.uk/20140328145127/http://www.environment-agency.gov.uk/static/documents/Business/6th_Dec_-_Shale_gas_-_North_West_-_Monitoring_of_flowback_water_-_update_(3).pdf)
710 [_Monitoring_of_flowback_water_-_update_\(3\).pdf](http://webarchive.nationalarchives.gov.uk/20140328145127/http://www.environment-agency.gov.uk/static/documents/Business/6th_Dec_-_Shale_gas_-_North_West_-_Monitoring_of_flowback_water_-_update_(3).pdf), (accessed October 2017).

711 (65) T.L. Tasker, W.D. Burgos, P. Piotrowski, L. Castillo-Meza, T.A. Blewett, K.B. Ganow,
712 A. Stallworth, P.L. Delompré, G.G. Goss, L.B. Fowler, and J.P. Vanden Heuvel, Environmental

713 and Human Health Impacts of Spreading Oil and Gas Wastewater on Roads, *Environ. Sci.*
714 *Technol.*, 2018, **52**, 7081-7091.

715 (66) M.G. Fowler, L. D. Stasiuk, M. Hearn, and M. Obermajer, Devonian hydrocarbon source
716 rocks and their derived oils in the Western Canada Sedimentary Basin. *Bulletin of Canadian*
717 *Petroleum Geology*, 2001, **49**, 117-148.

718 (67) S.E. Arthur, P.V. Brady, R.T. Cygan, H.L. Anderson, and H.E. Westrich, Irreversible
719 sorption of contaminants during ferrihydrite transformation, *Proceedings of the Waste*
720 *Management Conference*, WM 1999, **99**, 1-14.

721 (68) R.S. Taylor, B. Stobo, G. Niebergall, R. Aguilera, J. Walter and E. Hards, Optimization
722 of Duvernay fracturing treatment design using fully compositional dual permeability numeric
723 reservoir simulation, SPE/CSUR Unconventional Resources Conference, Society of Petroleum
724 Engineers, Canada, September 30, 2014.

725 (69) D. Parkhurst, and C.A.J. Appelo, PHREEQC (Version 3)-A Computer Program for
726 Speciation. Batch-Reaction, One-Dimensional Transport, and Inverse Geochemical Calculations,
727 US Geologic Survey, Water Resources Division, Denver, CO, 2013.

728 (70) A.E. Booker, M.A. Borton, R.A. Daly, S.A. Welch, C.D. Nicora, D.W. Hoyt, T. Wilson,
729 S.O. Purvine, R.A. Wolfe, S. Sharma, and P.J. Mouser, 2017. Sulfide generation by dominant
730 Halanaerobium microorganisms in hydraulically fractured shales, *mSphere*, 2017, **2(4)**,
731 pp.e00257-17.

732 (71) N.R. Warner, T.M. Kresse, P.D. Hays, A. Down, J.D. Karr, R.B. Jackson, and A.
733 Vengosh, A. (2013). Geochemical and isotopic variations in shallow groundwater in areas of the

734 Fayetteville Shale development, north-central Arkansas, *Applied Geochemistry*, 2013, **35**, 207-
735 220.

736 (72) T. Hayes and B.F. Severin, Barnett and Appalachian shale water management and reuse
737 technologies, Report No. 08122-05, Research partnership to secure energy for America, 2012,
738 [https://edx.netl.doe.gov/dataset/barnett-and-appalachian-shale-water-management-and-reuse-](https://edx.netl.doe.gov/dataset/barnett-and-appalachian-shale-water-management-and-reuse-technologies/resource_download/d167805d-9a16-40b8-b3fb-123ac3edab20)
739 [technologies/resource_download/d167805d-9a16-40b8-b3fb-123ac3edab20](https://edx.netl.doe.gov/dataset/barnett-and-appalachian-shale-water-management-and-reuse-technologies/resource_download/d167805d-9a16-40b8-b3fb-123ac3edab20), (Accessed
740 November 2018)

741 (73) J.S. Rosenblum, K.A. Sitterley, E.M. Thurman, I. Ferrer, and K.G. Linden,. Hydraulic
742 fracturing wastewater treatment by coagulation-adsorption for removal of organic compounds
743 and turbidity. *Journal of environmental chemical engineering*, 2016, **4(2)**, 1978-1984.

744 (74) J. Webster, Haynesville Shale, *American Association of Drilling Engineers*, Chesapeake
745 Energy, 2009, [http://www.aade.org/app/download/7021874804/AADE+-](http://www.aade.org/app/download/7021874804/AADE+-+Haynesville+Shale+Drilling+%28Chesapeake%29.pdf)
746 [+Haynesville+Shale+Drilling+%28Chesapeake%29.pdf](http://www.aade.org/app/download/7021874804/AADE+-+Haynesville+Shale+Drilling+%28Chesapeake%29.pdf), (Accessed November 2018)

747 (75) L. Wang, Z. Dong, and Z. Xia, A multi-scale flow model for production performance
748 analysis in shale gas reservoirs with fractal geometry, *Scientific Reports*, 2018, **8(1)**, 11464.

749 (76) O.O. Adekunle and B.T. Hoffman, Minimum Miscibility Pressure Studies in the Bakken,
750 In *SPE Improved Oil Recovery Symposium*, Society of Petroleum Engineers 2014.

751 (77) P.H Nelson and S.L. Santus, Gas, oil, and water production from Wattenberg Field in the
752 Denver Basin, Colorado, *US Geological Survey Open-File Report*, 2011-1175, 2011.

753 (78) S.K. Juniper, and Y. Fouquet, Filamentous iron-silica deposits from modern and ancient
754 hydrothermal sites, *Can. Mineral.*, 1988, **26**, 859-869.

755 (79) K.O. Konhauser, and F.G. Ferris, Diversity of iron and silica precipitation by microbial
756 mats in hydrothermal waters, Iceland: Implications for Precambrian iron formations, *Geology*,
757 1996, **24**, 323-326.

758 (80) R.M. Cornell and U. Schwertmann, Influence of organic anions on the crystallization of
759 ferrihydrite, *Clay and Clay Minerals*, 1979, **27**, 402-410.

760 (81) A.M. Jones, R.N. Collins, J. Rose, and T.D. Waite, The effect of silica and natural
761 organic matter on the Fe(II)-catalysed transformation and reactivity of Fe(II) minerals, *Geochim.*
762 *Cosmochim. Acta*, 2009, **73**, 4409-4422.

763 (82) D. Perret, J.F. Gaillard, J. Dominik, and O. Atteia, The diversity of natural hydrous iron
764 oxides, *Environ. Sci. Technol.*, 2014, **34**, 3540-3546.

765 (83) K. Eusterhues, T. Rennert, H. Knicker, I. Kogel-Knabner, K.U. Totsche, and U.
766 Schwertmann, Fractionation of organic matter due to reaction with ferrihydrite: coprecipitation
767 versus adsorption, 2011, **45**, 527-533.

768 (84) C. He, and R.D. Vidic, Impact of antiscalants on the fate of barite in the unconventional
769 gas wells, *Environmental Engineering Science*, 2014b, **33**, 745-752.

770 (85) C.W. Blout, Barite solubilities and thermodynamic qualities up to 300° C and 1400 bars,
771 *Am. Mineral.*, 1977, **62**, 942-957.

772 (86) B.Y. Zhen-Wu, K. Dideriksen, J. Olsson, P.J. Raahauge, S.L.S. Stipp, and E.H. Oelkers
773 Experimental determination of barite dissolution and precipitations rates as a function of
774 temperature and aqueous fluid composition, *Geochim. Cosmochim. Acta*, 2016, **194**, 193-210.

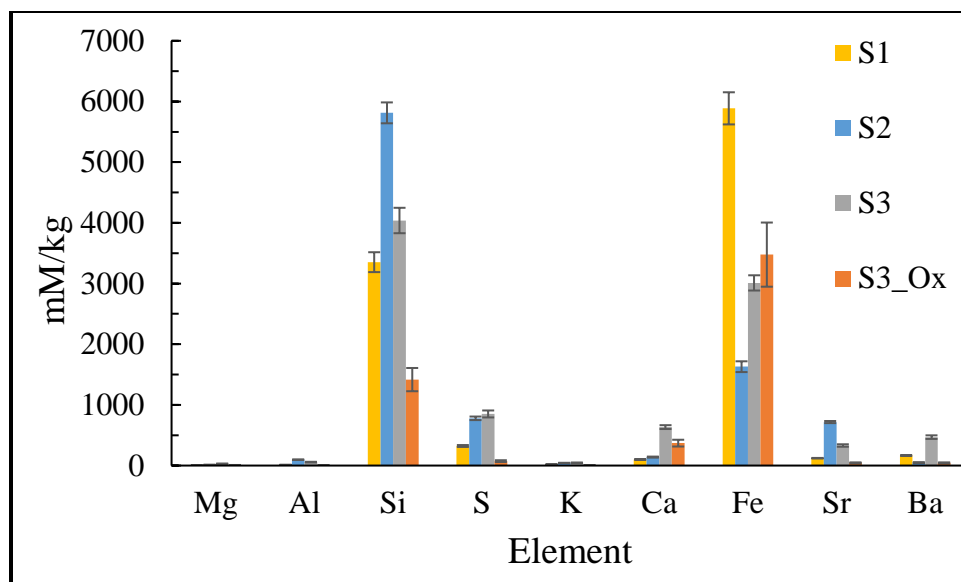
- 775 (87) P. Risthaus, D. Bosbach, U. Becker, and A. Putnis, Barite scale formation and dissolution
776 at high ionic strength studied with atomic force microscopy, *Colloids and Surf.*, 2001, **191**, 201-
777 214.
- 778 (88) K. Nielson, Y. Kalmykova, A.M. Stromvall, B. Anders, and E. Eriksson, Particle phase
779 distribution of polycyclic aromatic hydrocarbons in stormwater- using humic acid and iron nano-
780 sized colloids as test particles, *Sci. Total Environ.*, 2015, **532**, 103-111.
- 781 (89) A. Kondash, N.R. Warner, O. Lahav, and A. Vengosh, Radium and barium removal
782 through blending hydraulic fracturing fluids with acid mine drainage, *Environ. Sci. Technol.*,
783 2014, **48**, 1334-1342.
- 784 (90) C. He, M. Li, W. Liu, E. Barbot, and R.D. Vidic, Kinetics and equilibrium of barium and
785 strontium sulfate formation in Marcellus shale flowback water, *J. Environ. Eng.*, 2013, **140**,
786 B4014001.
- 787

788 Table 1 Summary of the aqueous chemistry for the three samples analyzed in this study.
789 Reported concentrations and detection limits (DL) are in ppm unless otherwise noted. BDL
790 denotes below detection limit and NM indicates the parameter was not measured for the
791 corresponding sample. In brackets, the relative standard deviation for each analysis is presented
792 as the percent within one deviation.

	DL	S1*	S2 [#]	S3
TDS		243,000	183,000	171,000
pH		4.78	5.86	5.51
Alkalinity (as CaCO ₃)	NM	2.25	14.3	54.4
T (C°) at collection		60	NM	38
TOC	0.46	212	737	294
TN	0.27	498	425	410
Cl	0.04	136,000	107,000	112,000
Na	0.33	70,000	59,500	54,300
Ca	1.13	11,800	6,500	8,630
K	1.47	2,570	2,160	1,930
Sr	0.049	1,470	931	904
Br	0.24	276	297	242
Fe	0.23	22	1.19	151
S	0.18	64.5	66.9	78.3
Si	0.37	7.9	BDL	BDL
Ba	0.00022	5.85	7.28	24.1
SO ₄ ²⁻	0.2	48.7	BDL	BDL
Li	0.00038	54.6	51.3	41.3
B	0.021	71.6	96	79.1
Mg	0.090	111	706	738
Mn	0.00090	15.8	7.32	15.1
Ni	0.0055	BDL	BDL	BDL
Cu	0.01	BDL	BDL	BDL
Zn	0.018	4.4	1.24	0.561
As	0.0050	BDL	BDL	BDL
Cd	0.00013	BDL	BDL	BDL
Pb	0.00014	0.06	BDL	BDL

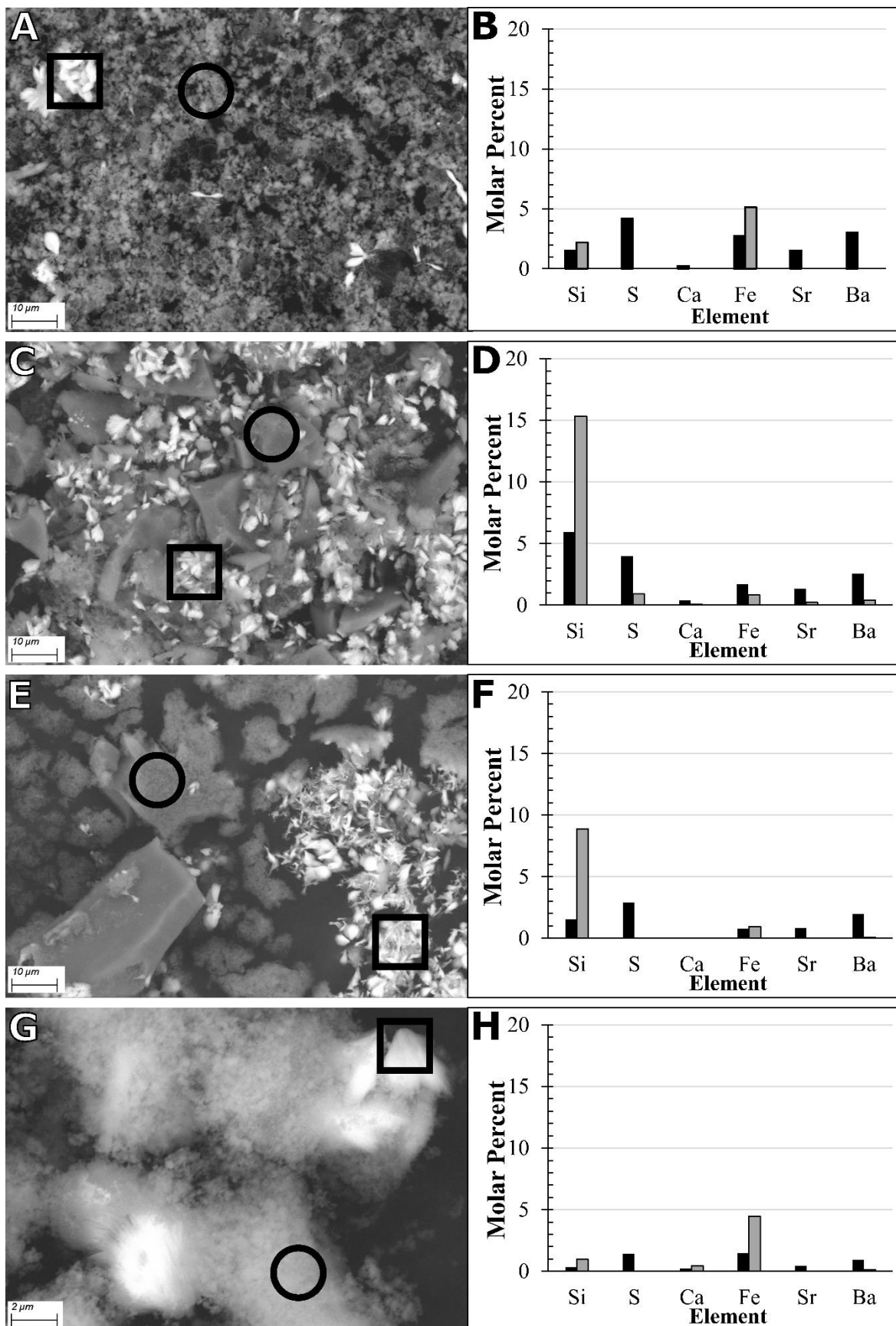
793

794 The chemistry of S1 and S2 were previously reported in *He et al.¹; #Blewett et al.⁵⁰,
795 respectively, with the new analyses being conducted for alkalinity and total sulfur for both and
796 Pb, Cu, and Si for S2.

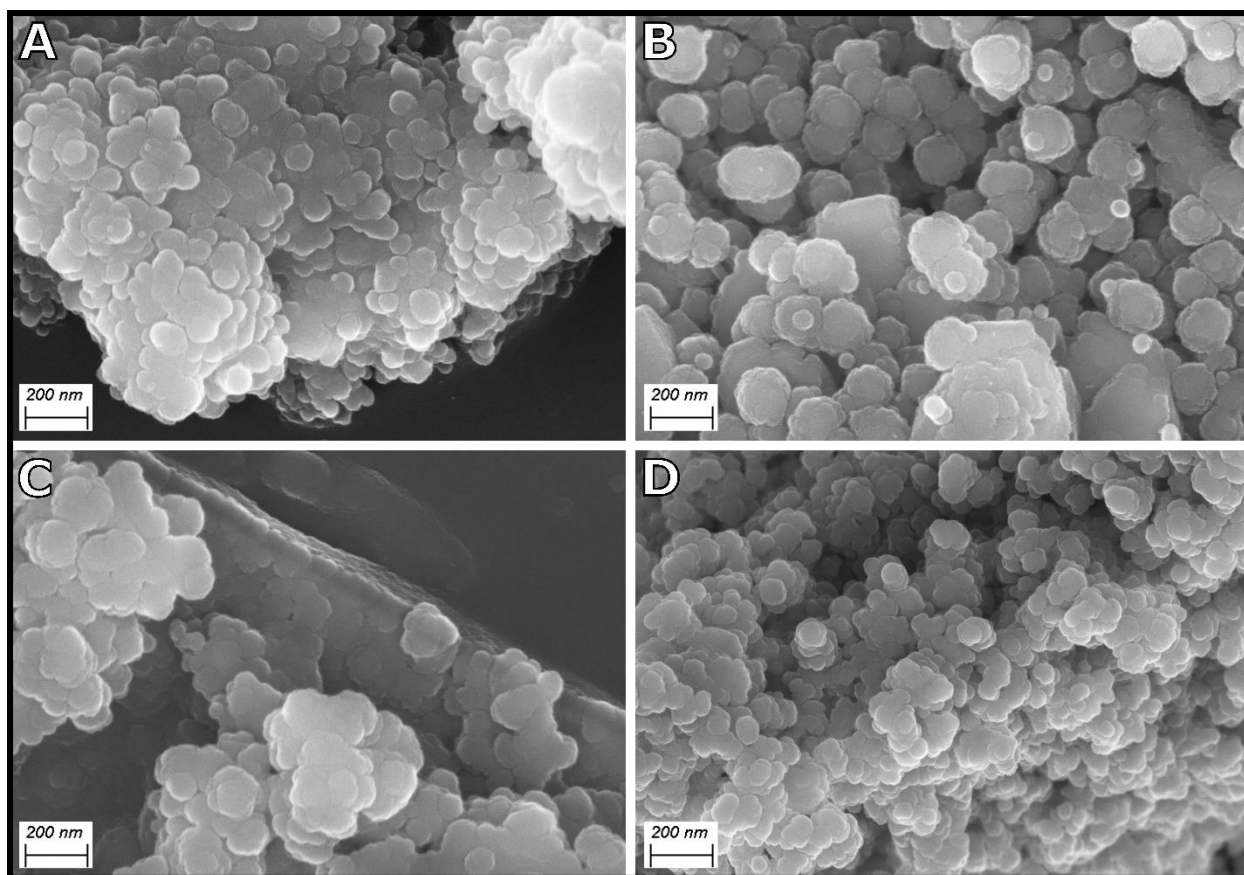


797

798 Figure 1 Elemental profile of FPW solids as determined through alkaline fusion digestion, in
 799 with the error bars representing ± 1 standard deviation.



801 Figure 2. SEM images in backscatter mode and elemental distribution determined by EDS of
802 samples S1 A) and B), S2 C) and D), S3 E) and F), and S3_Ox G) and H). In each SEM image
803 the square and circle represent the location from which the EDS spectra was acquired and
804 correspond to the black and white bars in the corresponding elemental distributions as molar
805 percent, respectively.

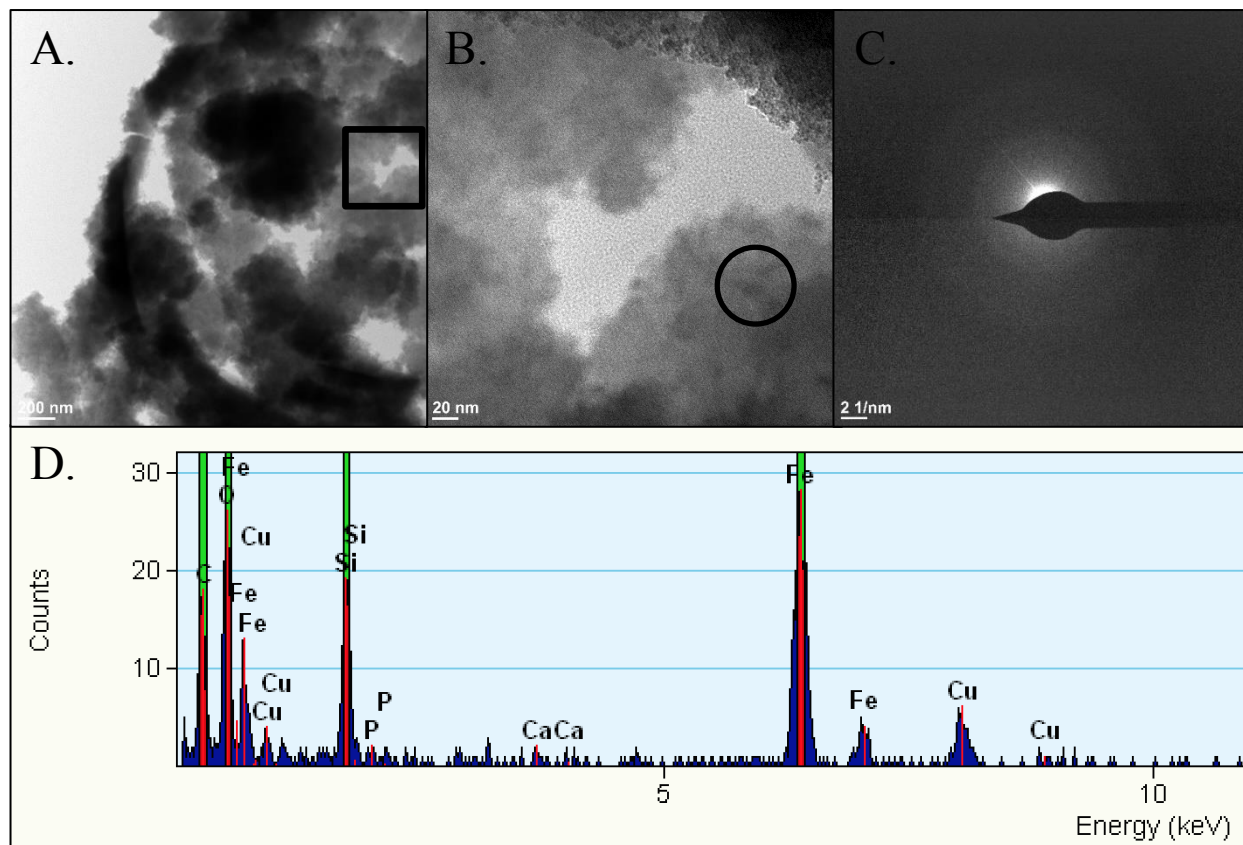


806
807 Figure 3. High resolution SEM images of carbon coated samples showing the morphology of
808 Fe/Si globular neoformed aggregates associated solids: A) S1, B) S2, C) S3, and D) S3_Ox.

809

810

811



812 Figure 4. TEM analysis of solids of S1. A) A wide image in which the square represents the
 813 location of the close-up image in panel B). B) is a close-up image in which the circle represents
 814 the approximant location of the SAED spectra presented in panel C) and EDS spectra presented
 815 in panel D).

816

817

818

819

820

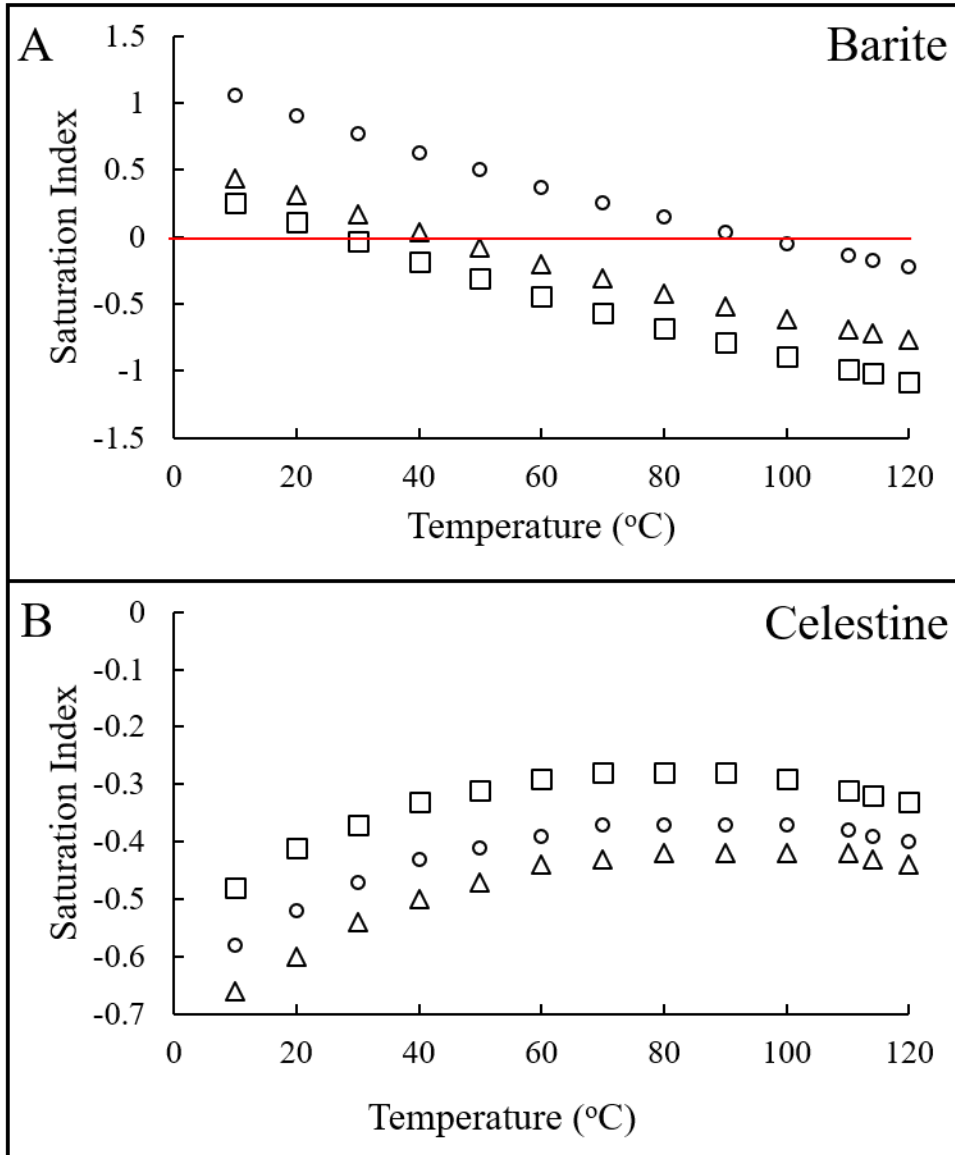
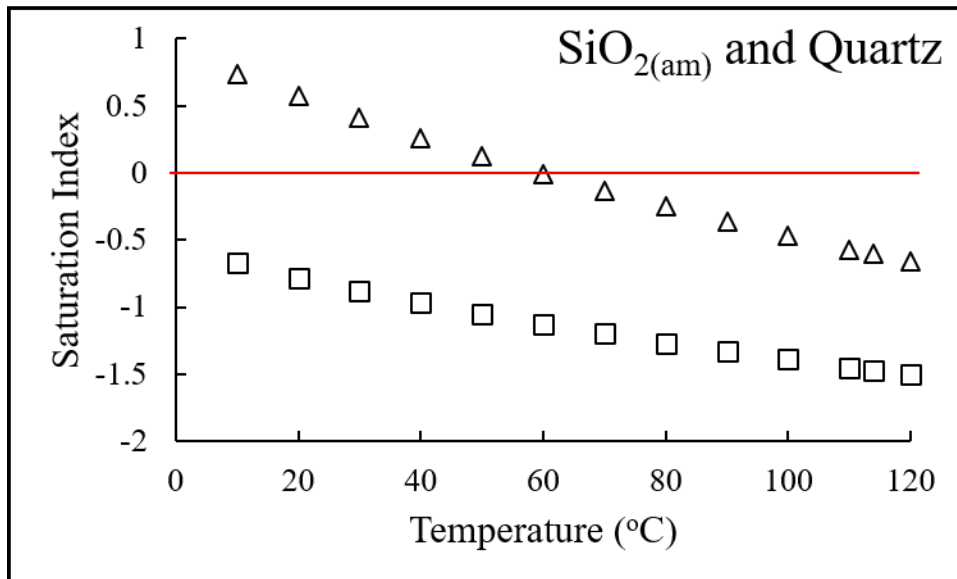


Figure 5. Saturation indices of hypothesized minerals present in Duvernay FPW modeled using the element data as a function of temperature A) respect to barite, and B) celestine, with S1, S2, and S3 represented by (\square), (Δ), and (\circ), respectively.



827

828 Figure 6. Saturation indices of potential silicate minerals present in Duvernay FPW modeled
 829 using the element data from S1 as a function cooling for SiO_{2(am)} (□), and quartz (Δ).

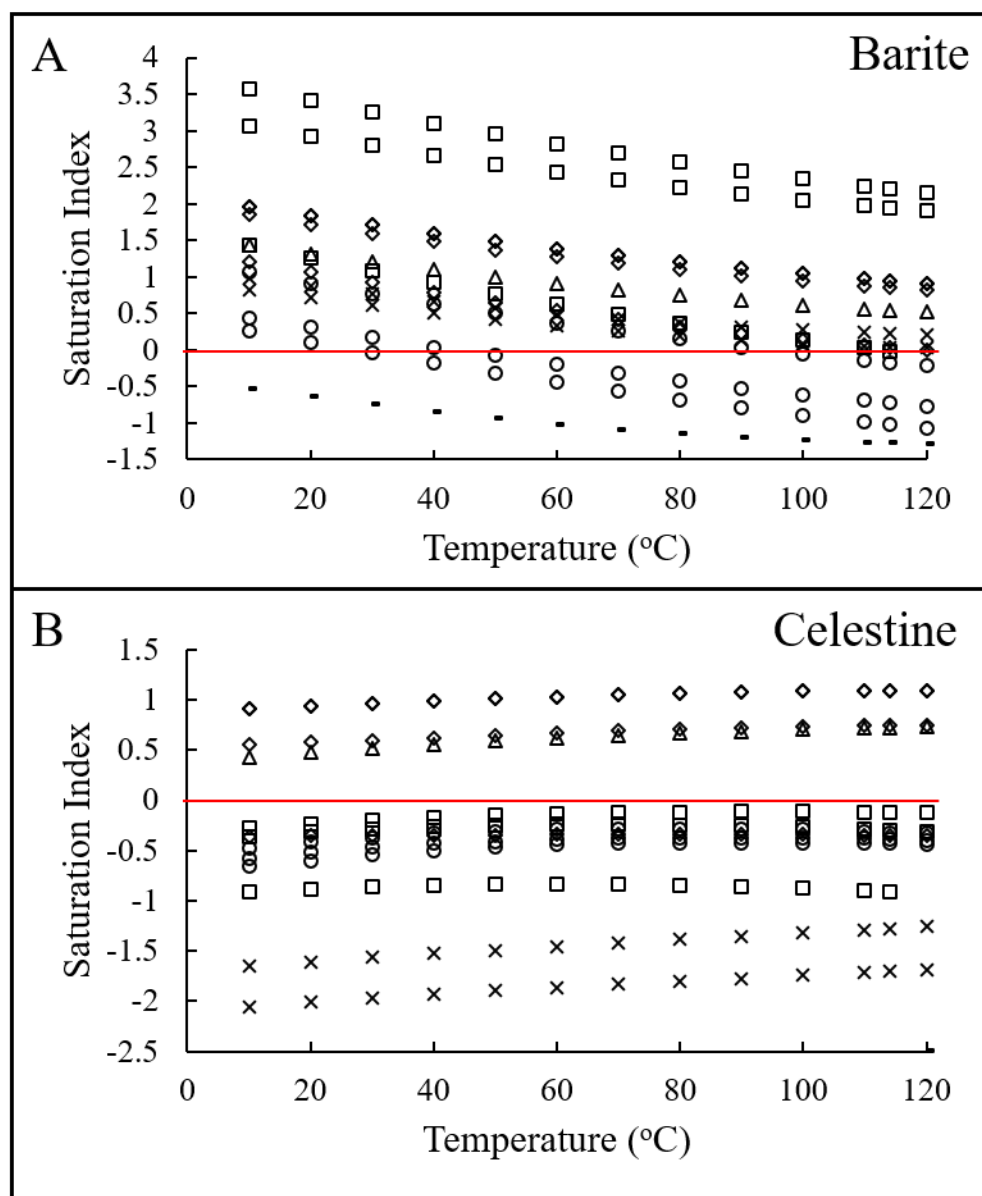
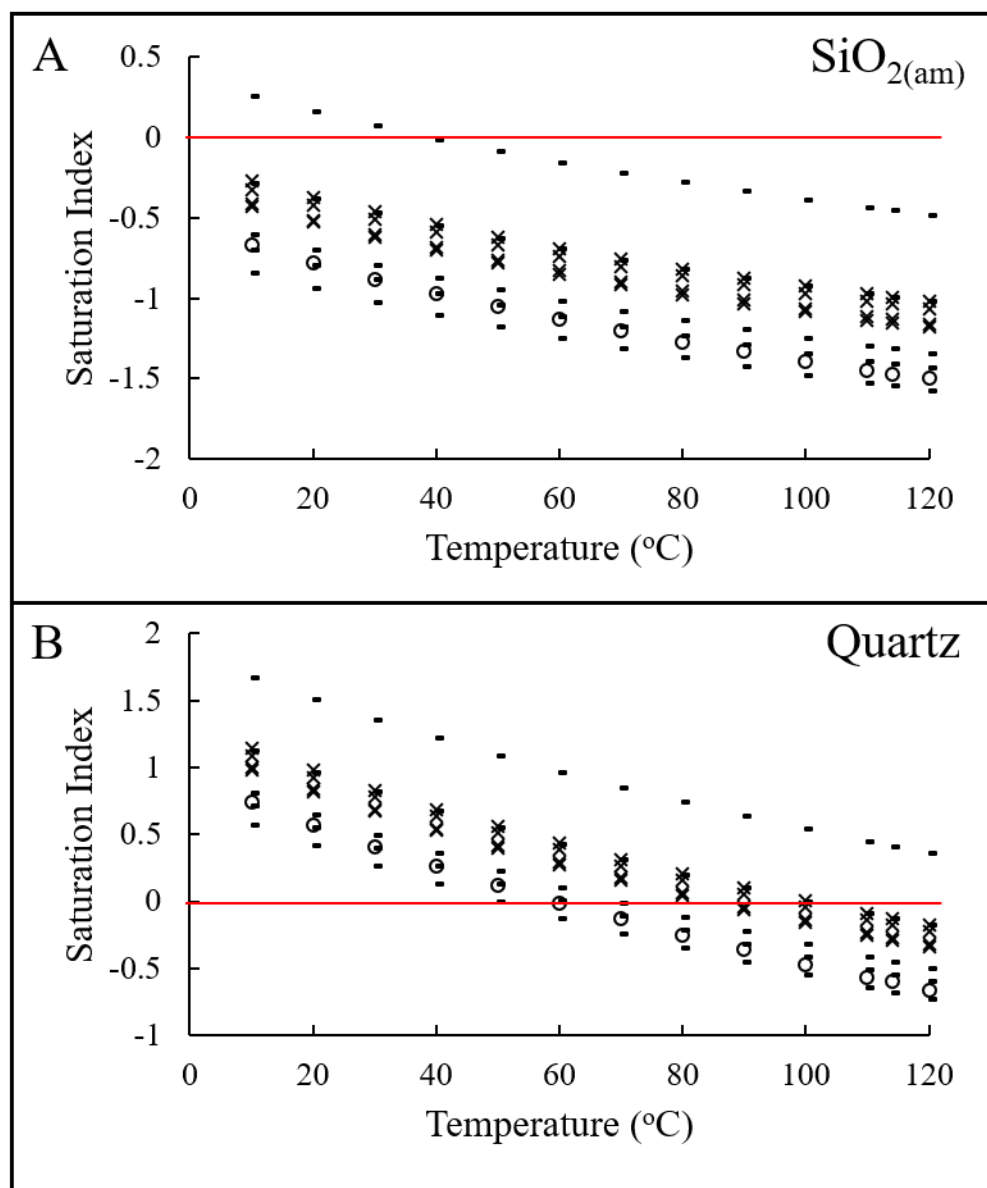


Figure 7. A cross basin comparison of saturation indices of FPW for A) barite and B) celestine as a function of temperature for the Duvernay, Marcellus, Barnett, Bakken, Denver-Julesburg, and Fayetteville (\circ), (\square), (Δ), (\diamond), (\times) and (-), respectively.

835

836



837

838 Figure 8. A cross basin comparison of saturation indices of FPW for A) $\text{SiO}_{2(\text{am})}$ and B) quartz as
 839 a function of temperature for the Duvernay, Bakken, Denver-Julesburg, and Fayetteville (○), (Δ),
 840 (×) and (-), respectively.

841

Supplementary Information

Characterization and Implications of Solids Associated with Hydraulic Fracturing Flowback and
Produced Water from the Duvernay Formation, Alberta, Canada

Shannon L. Flynn^{1,2*}, Konstantin von Gunten², Tyler Warchola², Katherine Snihur², Tori Z.
Forbes³, Greg G. Goss⁴, Murray K. Gingras², Kurt O. Konhauser², and Daniel S. Alessi².

¹*School of Natural and Environmental Sciences,*

Newcastle University, Newcastle upon Tyne, NE1 7RU, UK

²*Department of Earth and Atmospheric Sciences,*

University of Alberta, Edmonton, AB T6G 2E3, Canada

³*Department of Chemistry*

University of Iowa, Iowa City, IA, 52242, USA

⁴*Department of Biological Sciences,*

University of Alberta, Edmonton, AB T6G 2E3, Canada

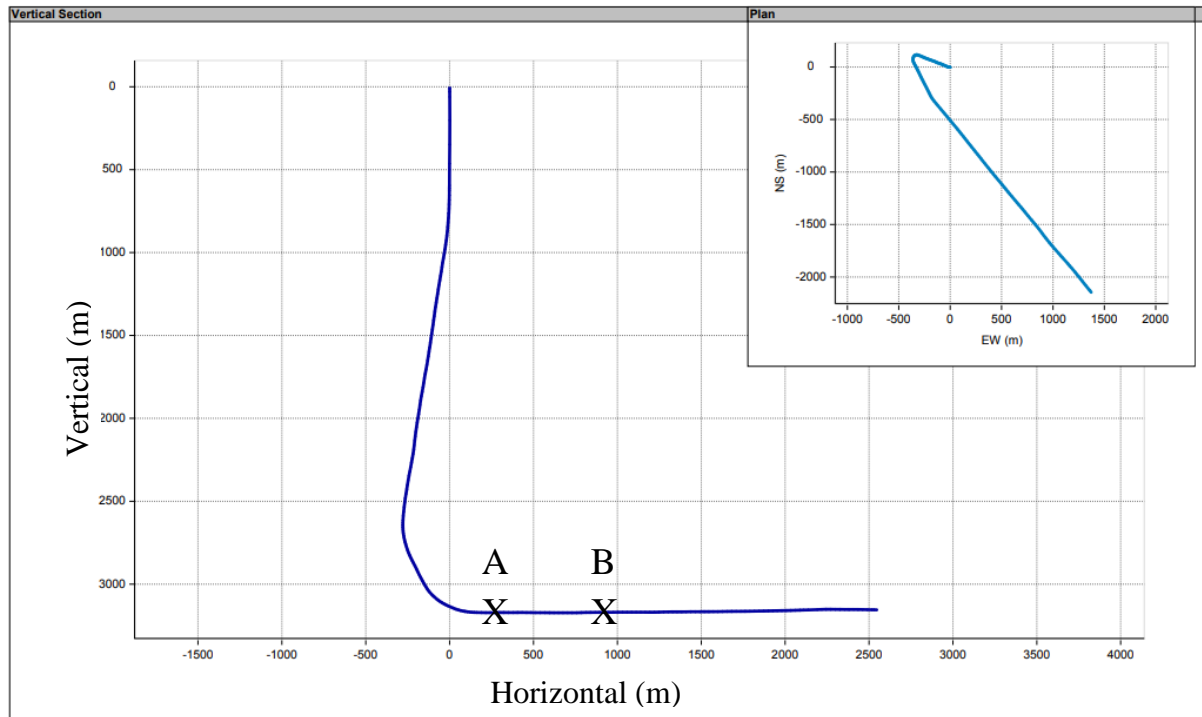
* Corresponding Author: shannon.flynn@ncl.ac.uk

Duvernay Formation Geology and Composition

The Frasnian Duvernay Formation (Woodbend Group) is a bituminous and variably calcareous mudstone that is present throughout most of the Western Canada Sedimentary Basin. The Duvernay Formation is laterally equivalent to the Leduc Formation, a carbonate platform and reef complex that has been exploited for conventional oil and gas since 1947. The Geology of the Duvernay Formation is summarized in Stoakes¹. The Duvernay Formation comprises Interbedded bituminous shales, dark brown, calcareous shales and dense argillaceous limestones. More rarely observed are fossil-rich lime mud accumulations. The bituminous shales are characteristically plane-parallel laminated. Argillites are also planar laminated, but may also be massive appearing or completely bioturbated. The variability in bedding is best interpreted as unsteadiness in oxygenation further suggesting that redox-sensitive elements are heterogeneously distributed. The shales and the argillites contain — in descending abundance — silt-sized quartz, mica, K-feldspar, and plagioclase; the clay-size fraction is dominantly quartz and calcite with subordinate clay illite/smectite and less abundant kaolinite^{2,3}. Total organic content is variable, locally exceeding 10% and more commonly between 1 and 3%⁴. Eogenetic to diagenetic pyrite is locally common. Barite, likely from hydrothermal sources, is present up to 1.4 weight %³.

Profile of Well 3

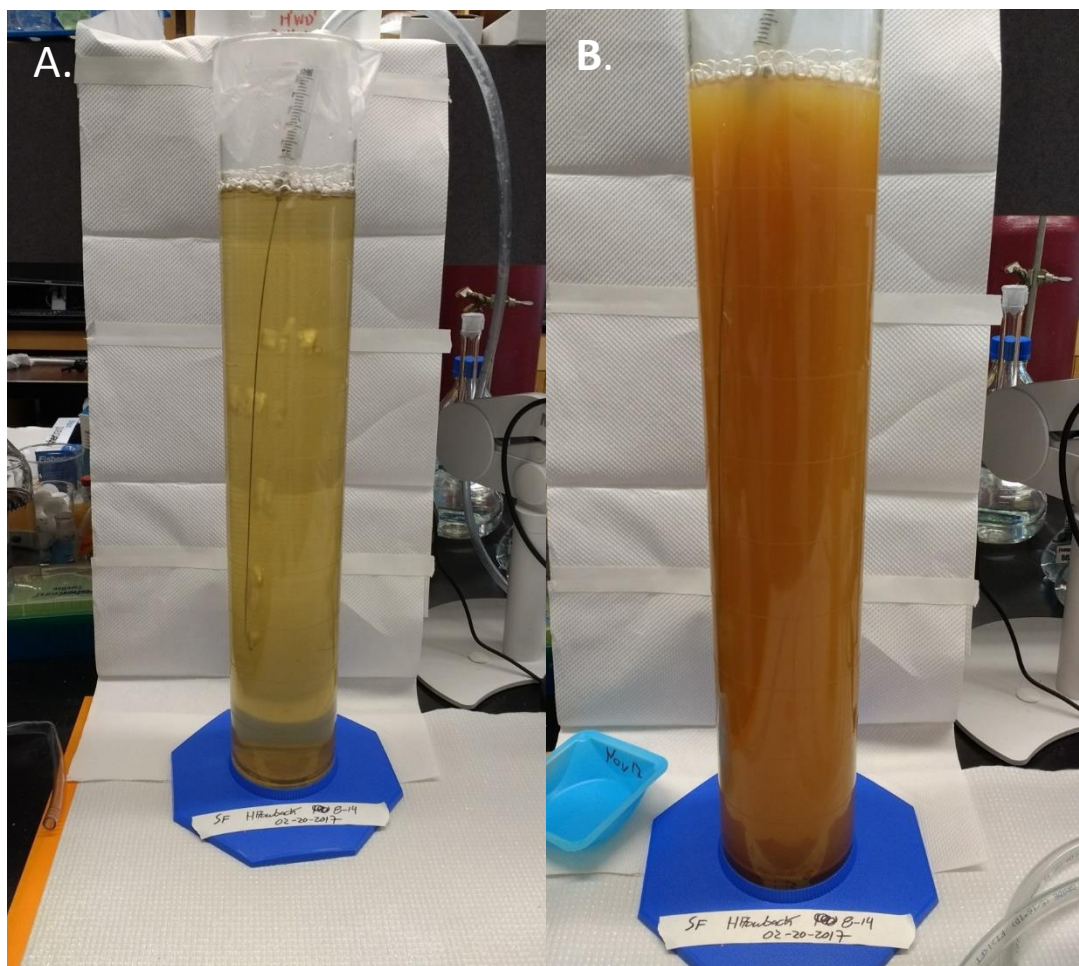
Well 3 was drilled into the Duvernay Formation at a depth of 3172 m with a horizontal bore length of 2535. Sample A came from 139 m into the horizontal bore while B came from 839 m (Figure SI.1)



880

881 Figure SI.1 Schematic of well 3's bore showing the approximant locations from where drill

882 cutting samples A and B were obtained.



883 Figure SI.2 Sample S3 before (A) and after bubbling (B).

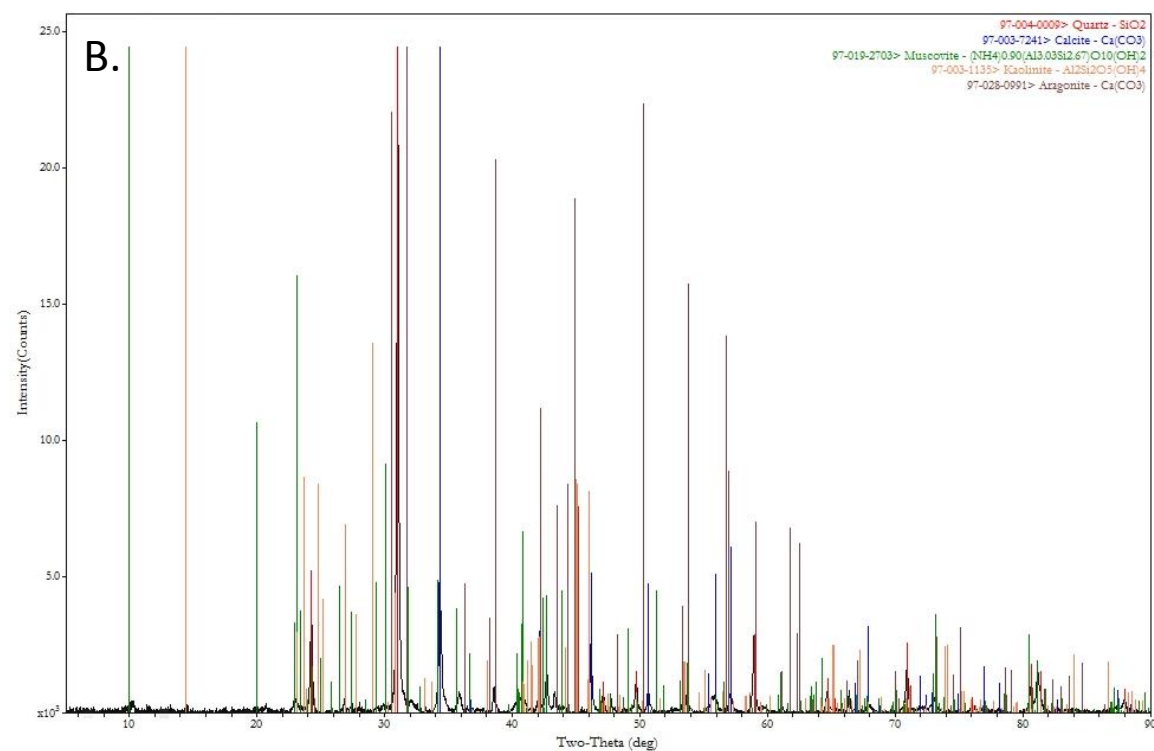
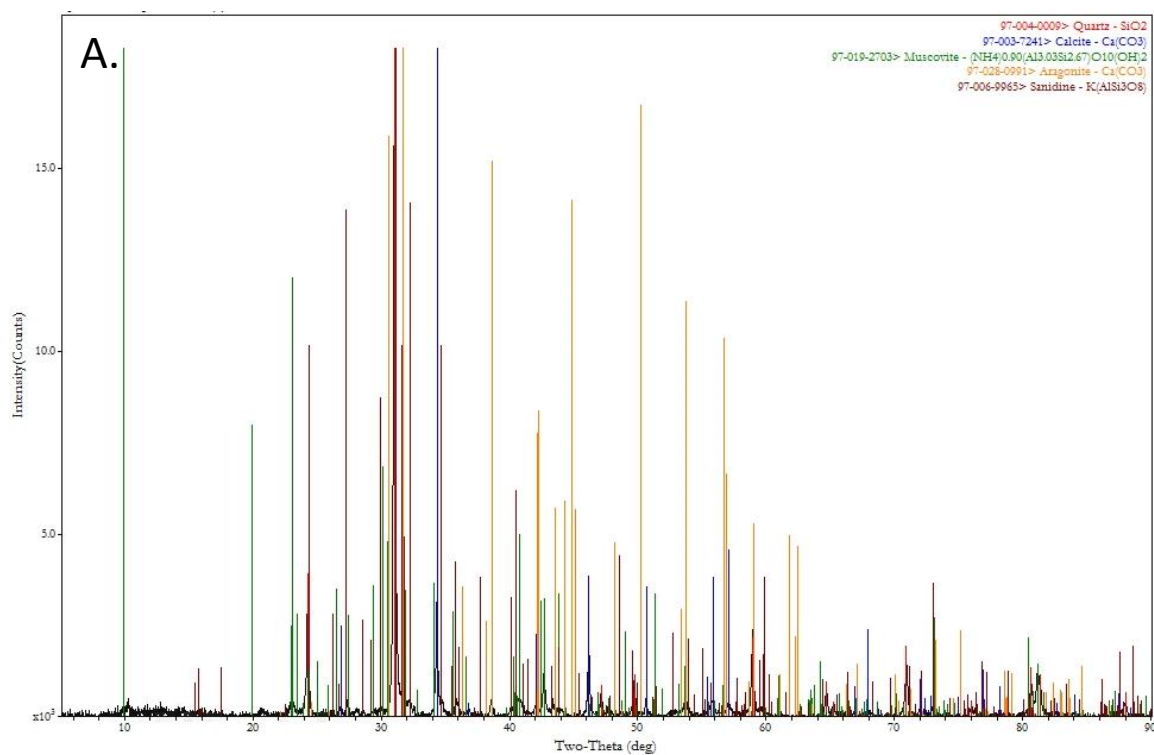


Figure SI.3 XRD spectra of the bulk mineralogy from drill cuttings from well 3's lateral bore A) 3550 m and B) 4250 m.

Table SI.1 The elemental composition of the FPW associated solids in mM as determined by alkaline fusion digestions and the associated relative standard deviation (RSD) as determined through three replicate digestions.

	S1	RSD	S2	RSD	S3	RSD	S3_Ox	RSD
Element	mM	%	mM	%	mM	%	mM	%
Mg	0.757	4.5	12.0	17.5	29.5	5.5	7.53	24.9
Al	10.7	30.0	96.9	3.8	57.0	8.8	2.17	37.2
Si	3,350	4.9	5,810	3.0	4,040	5.2	1,420	13.5
P	10.6	20.5	3.72	77.0	35.2	9.9	11.9	51.8
S	322	4.8	778	3.8	851	6.7	73.1	20.4
K	17.9	14.4	43.3	5.7	45.7	10.2	2.77	57.5
Ca	99.7	2.4	139	6.1	634	5.0	370	15.1
Mn	NM		1.74	3.9	NM		0.834	16.2
Fe	5,890	4.5	1,630	5.4	3,010	4.2	3,480	15.2
Zn	NM		2.44	46.6	NM		1.56	25.7
Sr	121	3.8	717	2.4	330	6.1	44.3	18.0
Ba	166	4.4	49.0	6.3	468	6.3	43.5	20.3

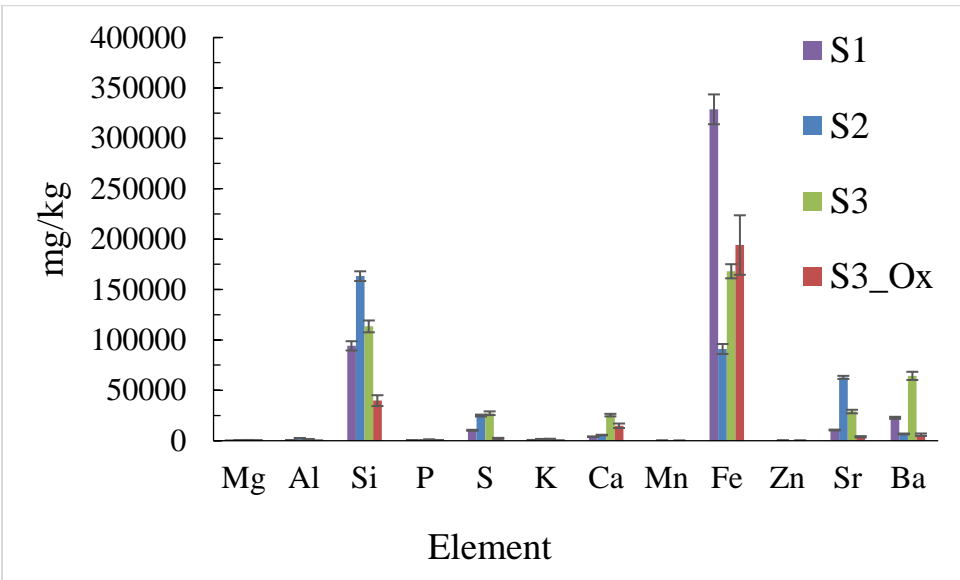
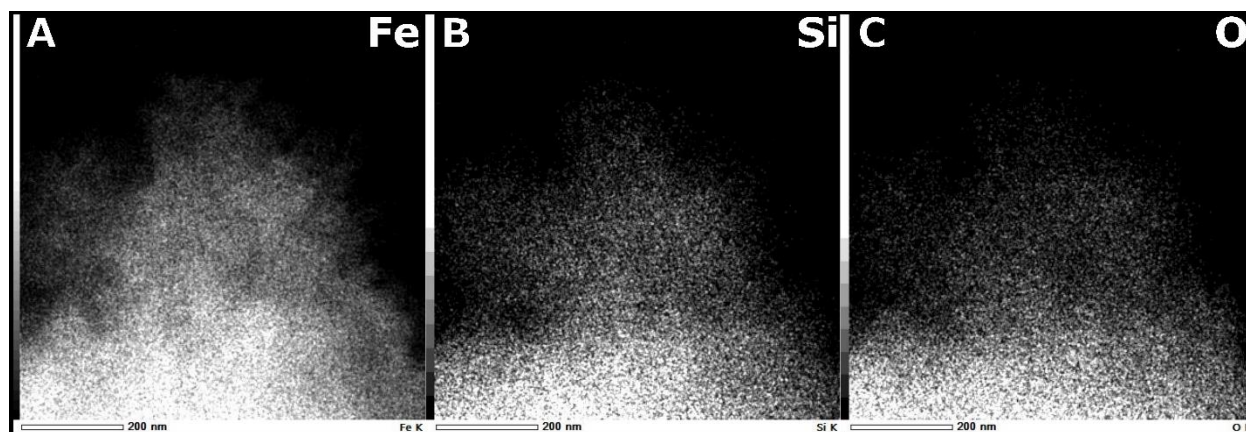


Figure SI.4 Elemental profile of FPW solids as determined through alkaline fusion digestion, in which the error bars represent ± 1 standard deviation.

896



897

898 Figure SI.5 STEM elemental maps of particle agglomerates from S1 showing the distribution of
899 A) Fe, B) Si, and C) O.

900

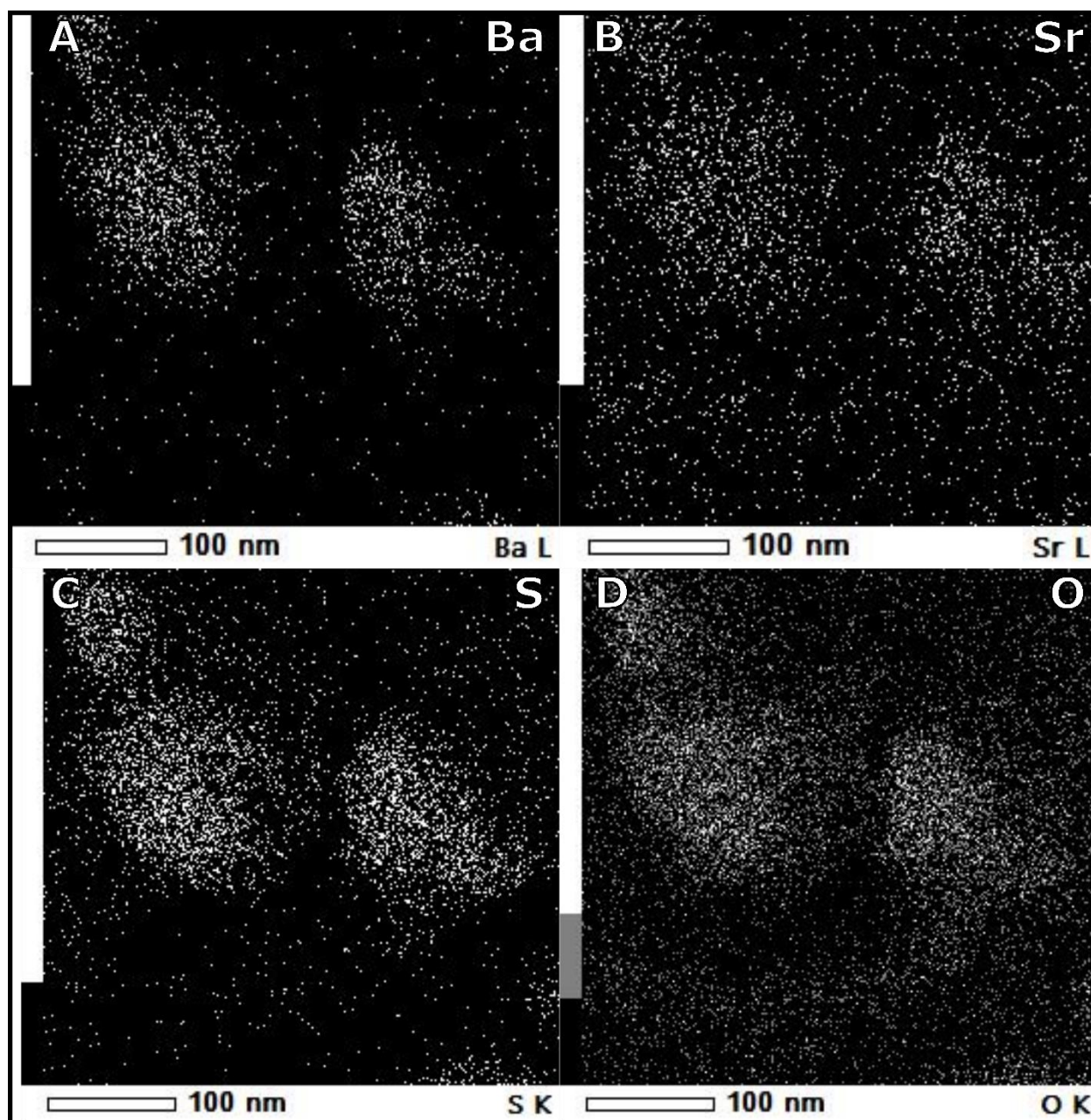


Figure SI.6 STEM elemental maps of particle agglomerates from S1 showing the distribution of A) Ba, B) Sr, C) S, and D) O.

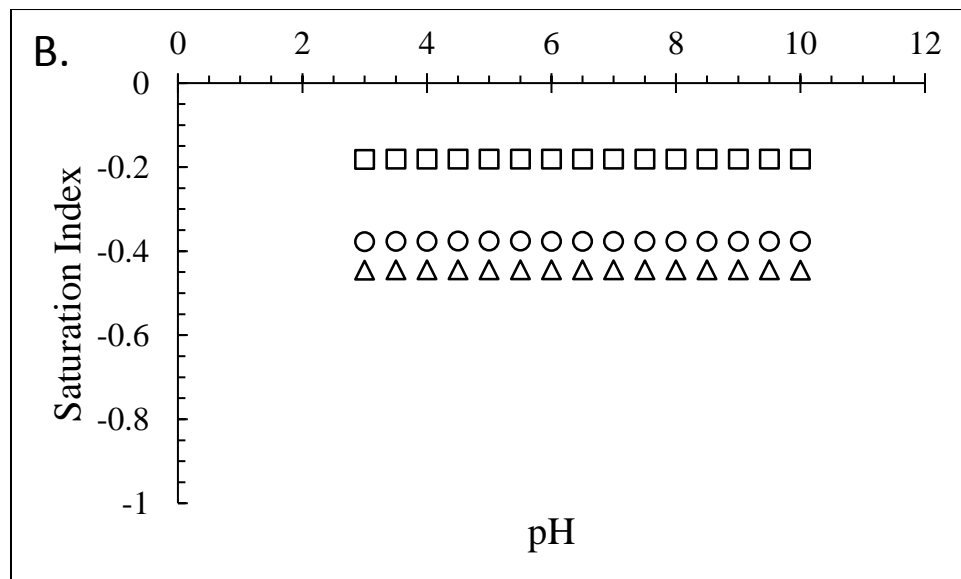
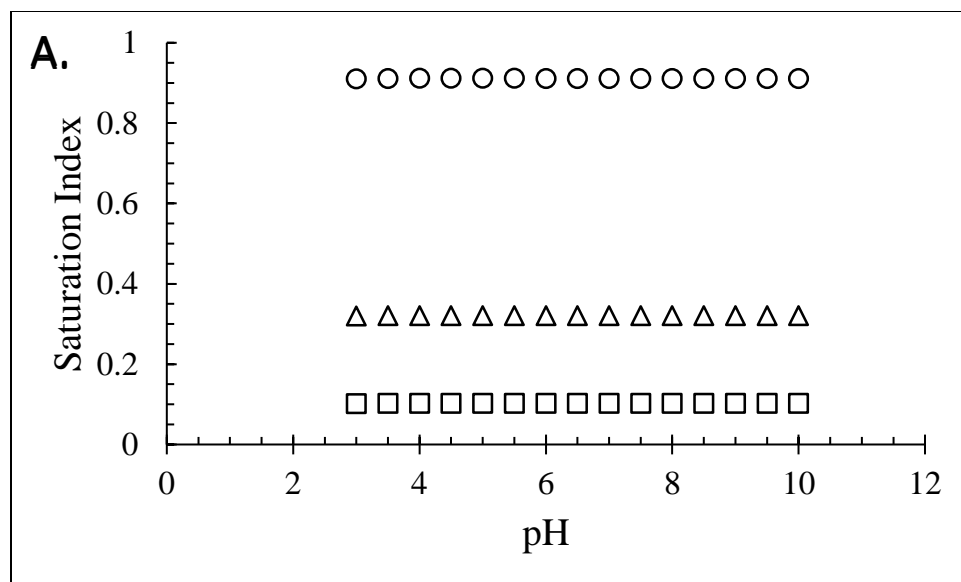
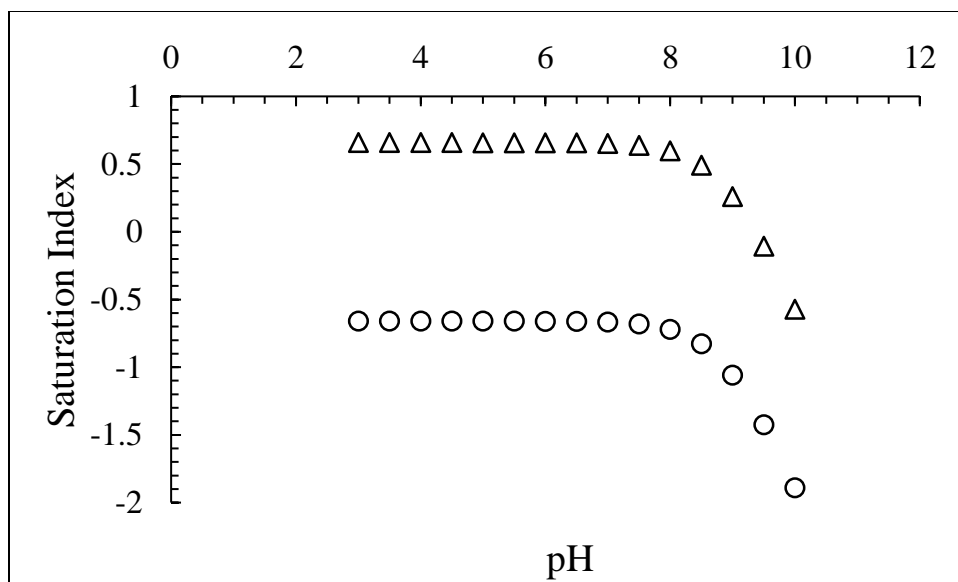
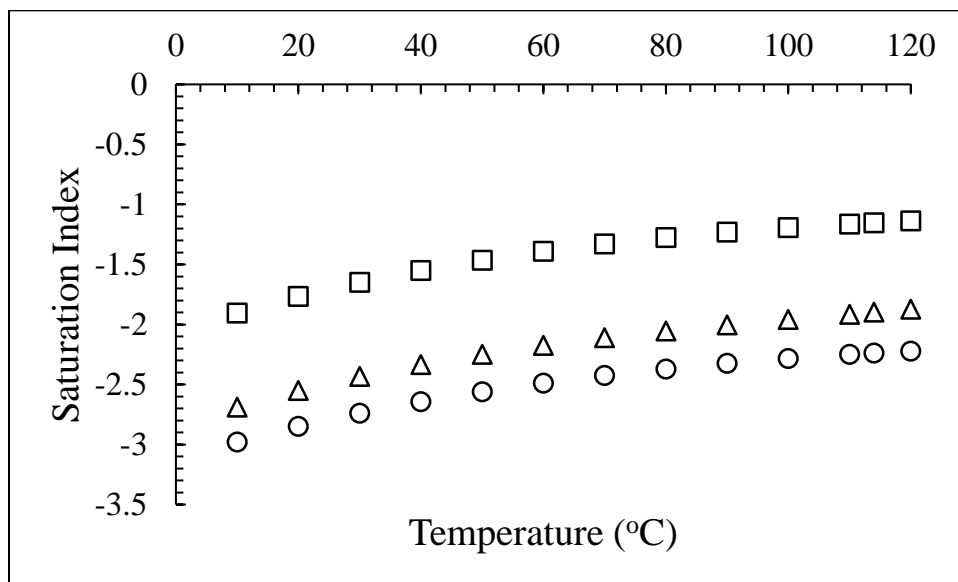


Figure SI.7 Saturation indices of hypothesized minerals present FPW modeled using the element data as a function of pH A) respect to barite, and B) celestine, with S1, S2, and S3 represented by (□), (Δ), and (○), respectively.

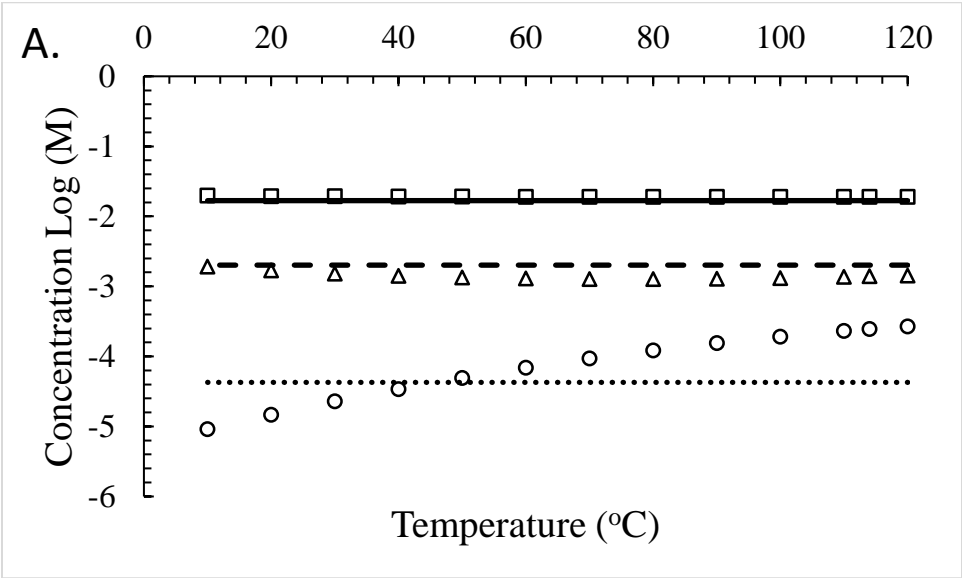


909
 910 Figure SI.8 Saturation indices of potential silicate minerals present FPW modeled using the
 911 element data from S1 as a function pH for SiO₂(am) (□), and quartz (Δ).

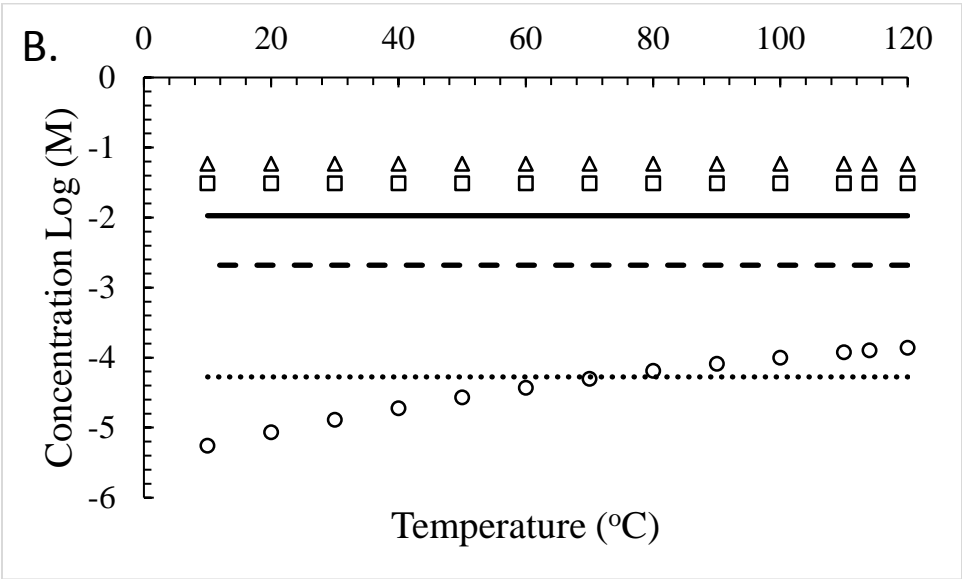


912
 913 Figure SI.9 Saturation indices of CO₂ modeled using the FPW chemistry as a function of
 914 temperature with samples S1, S2, and S3 represented by (□), (Δ), and (○), respectively.

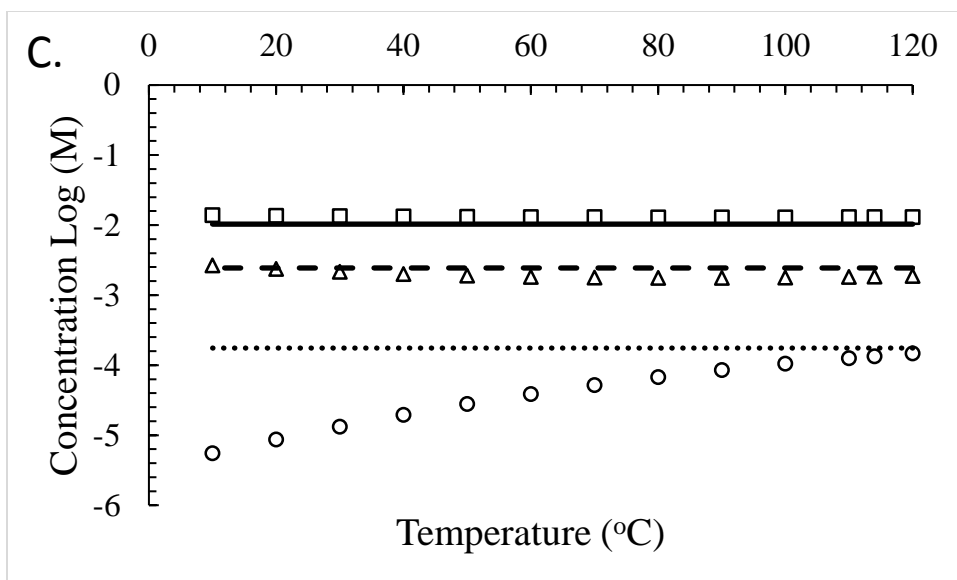
915



916



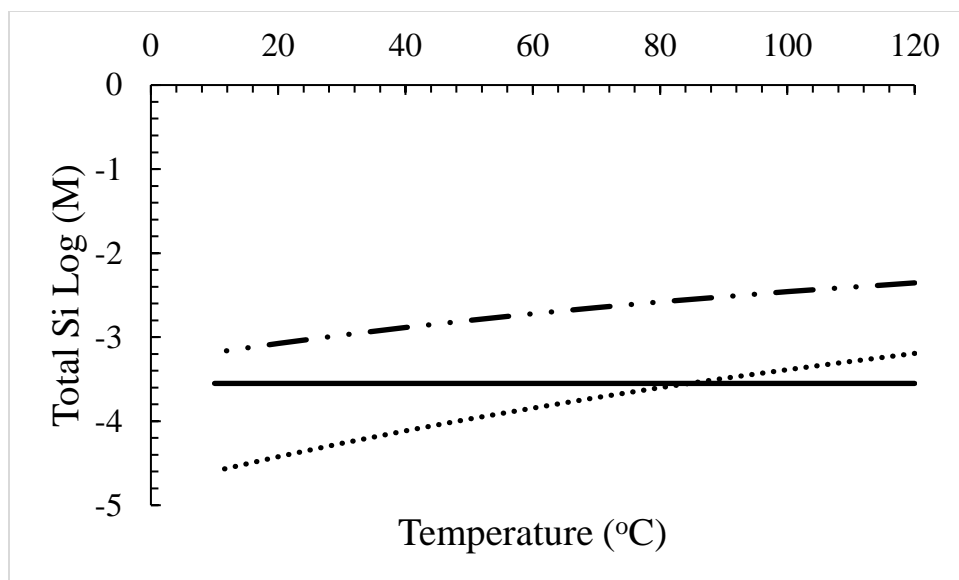
917



918

919 Figure SI.10 Comparison of the measured and model elemental concentrations in equilibrium
 920 with celestine and barite for A) S1, B) S2, and S3 in which the modeled Sr concentration is
 921 represented by (□), SO₄²⁻ by (Δ), and by Ba (○). The measured concentrations are for Sr, S, and
 922 Ba, represented by the solid, dashed and dotted lines respectively.

923



924
 925 Figure SI.11 Comparison of the measured and model elemental concentrations of Si for S1 in
 926 equilibrium with silica minerals quartz and $\text{SiO}_{2(\text{am})}$ as a function of cooling temperatures. The
 927 modeled concentrations of Si in equilibrium with quartz and $\text{SiO}_{2(\text{a})}$ are represented by the
 928 dotted, and dotted and dashed lines, respectively. The solid line represents the measured Si
 929 concentration for S1.

930 Table SI.2 Data used to model the saturation indices for barite (BaSO₄), celestine (SrSO₄), quartz (SiO₂), and amorphous silica
931 (SiO_{2(am)}) using FPW data from the Fayetteville, Bakken, Denver-Julesburg, Marcellus and Barnett Formations. NR denotes not
932 reported and ND denotes not detected.

		Ba	Br	Alkalinity as CO ₃ ²⁻	Ca		Fe	K	Mg	Mn	Na	SO ₄ ²⁻	Si	Sr	
Fayetteville	Site	(ppm)	(ppm)	(ppm)	(ppm)	Cl (ppm)	(ppm)	(ppm)	(ppm)	(ppm)	(ppm)	(ppm)	(ppm)	(ppm)	pH
Warner et al. ⁵	FS-1	5	96	1,136.6	221	5507	1	NR	56	2	3,232	ND	47	27	NR
	FS-2	4	122	486.0	345	10,165	13	NR	61	2	3,575	ND	13	14	NR
	FS-3	4	144	538.4	350	9,896	10	NR	75	3	4,607	ND	22	49	NR
	FS-4	3	101	874.6	386	10,312	1	NR	67	2	4,224	3	160	18	NR
	FS-5	3	97	800.0	284	6,771	8	NR	47	2	3,152	ND	18	26	NR
Bakken															
Shrestha et al. ⁶	PW1	9.2	558	17.5	12,033	119,989	19.2	NR	1001	16.7	47,217	128	NR	774	NR
	PW2	12.4	384	84.5	8,573	75,892	30.2	NR	741	13.1	34,745	102	NR	551	NR
	PW3	26.3	91.6	428	372	21,728	0.7	NR	118	0.2	12,271	NR	NR	33.1	NR
	PW4	6.4	601	NR	15,346	136,220	22.3	NR	1299	15.8	60,571	293	NR	970	NR
	FW1	10.5	NR	145.35	9,683.3	118,666	96	NR	1273.3	7.1	61,466	650	NR	764	NR
Denver-Julesburg															
Rosenblum et al. ⁷²	HF	41.39	191.6	235.04	550	17,497	2.71	51.6	71.4	1.03	10,461	8.5	31.96	78	6.84

	VF1	41.07	244.4	41.97	1,081	24,955	6	75.9	119.3	0.19	14,215	>0.05	42	179	6.59
	VF2	31.55	265.1	67.15	1,204	27,103	4.8	65.4	130	0.33	14,794	>0.05	29	202	6.93
	VF3	14.15	81.3	164.88	365.5	12,724	19	52.9	40.5	0.29	7472	26.63	41	47	6.93
Marcellus															
Haluszczak et al. ⁸		11,990	872	42.6	11,200	98,300	747	281	875	5.6	36,400	50	NR	2,330	6.2
Barbot et al. ⁹		2,224	511	99	7,220	57,447	40.8	0	632	0	24,123	71	NR	1,695	6.56
He et al. ¹⁰	A	730	NR	NR	2,170	29,000	NR	NR	249	NR	11,860	NR	NR	362	7.42
	B	236	NR	NR	15,021	104,300	NR	NR	1720	NR	27,946	14.8	NR	1799	6.4
Barnett															
Hayes and Severin ¹¹		3.6	589	441	1,600	34,700	24.9	316	255	0.86	18,850	709	NR	529	7.05

933 Warner et al.⁵: 5 Flowback water samples from the Fayetteville Formation.

934 Shrestha et al.⁶: 4 produced water and 1 flowback sample from the Bakken Formation.

935 Rosenblum et al.⁷: 4 total flowback samples, 1 from a horizontally fractured well and 3 from vertically fractured well from the
936 Wattenberg field in the Denver-Julesburg Basin.

937 Haluszczak et al.⁸: median concentration from day 14 flowback from 7 wells in the Marcellus Formation.

938 Barbot et al.⁹: average from 95 Marcellus flowback samples.

939 He et al.¹⁰: two composite samples from separate wells in the Marcellus Formation. Sample A is a composite of days 1, 5 and 7, while
940 sample B is a composite of FPW from days 1, 3, and 5.

941 Hayes and Severin¹¹: the median of samples from 4 wells in the Barnett Formation from days 10-12.

References

- (1) F.A. Stoakes, Nature and control of shale basin fill and its effect on reef growth and termination: Upper Devonian Duvernay and Ireton formations of Alberta. *Bulletin of Canadian Petroleum Geology*, 1980, **28**, 234-410.
- (2) S.D.A. Anderson, C. D. Rokosh, J.G. Pawlowicz, H. Berhane and A. P. Beaton, 2010, Mineralogy, permeametry, mercury porosimetry, pycnometry and scanning electron microscope imaging of Duvernay and Muskwa Formations in Alberta: Shale Gas Data Release: ERCB/AGS Open File 830 Report, https://ags.aer.ca/document/OFR/OFR_2010_02.pdf (Accessed November 2018).
- (3) M.R. Yassin, M. Begum, and H. Dehghanpour, Organic shale wettability and its relationship to other petrophysical properties: A Duvernay case study. *International Journal of Coal Geology*, 2017, **169**, 74-91.
- (4) M.G. Fowler, L. D. Stasiuk, M. Hearn, and M. Obermajer, Devonian hydrocarbon source rocks and their derived oils in the Western Canada Sedimentary Basin. *Bulletin of Canadian Petroleum Geology*, 2001, **49**, 117-148.
- (5) N.R. Warner, T.M. Kresse, P.D. Hays, A. Down, J.D. Karr, R.B. Jackson, and A. Vengosh, A. (2013). Geochemical and isotopic variations in shallow groundwater in areas of the Fayetteville Shale development, north-central Arkansas, *Applied Geochemistry*, 2013, **35**, 207-220.

- (6) N. Shrestha, G. Chilkoor, J. Wilder, V. Gadhamshetty, and J.J. Stone, Potential water resource impacts of hydraulic fracturing from unconventional oil production in the Bakken Shale, *Water Res.*, 2017, **108**, 1-24.
- (7) J.S. Rosenblum, K.A. Sitterley, E.M. Thurman, I. Ferrer, and K.G. Linden,. Hydraulic fracturing wastewater treatment by coagulation-adsorption for removal of organic compounds and turbidity. *Journal of environmental chemical engineering*, 2016, **4(2)**, 1978-1984.
- (8) L.O. Haluszczak, A.W. Rose, and L.R. Kump, Geochemical evaluation of flowback brine from Marcellus gas wells in Pennsylvania, USA, *Appl. Geochem.*, 2013, **28**, 55-61.
- (9) E. Barbot, N.S. Vidic, K.B. Gregory, and R.D. Vidic, Spatial and temporal correlation of water quality parameters of produced waters from Devonian age shale following hydraulic fracturing, *Environ. Sci. Technol.*, 2013, **47**, 2562-2569.
- (10) C. He, X. Wang, W. Liu, E. Barbot, and R.D. Vidic, Microfiltration in the recycling of Marcellus Shale flowback water: solids removal and potential fouling of polymeric microfiltration membranes, *J. Membr. Sci.*, 2014c, **462**, 88-95.
- (11) T. Hayes and B.F. Severin, Barnett and Appalachian shale water management and reuse technologies, Report No. 08122-05, Research partnership to secure energy for America, 2012, https://edx.netl.doe.gov/dataset/barnett-and-appalachian-shale-water-management-and-reuse-technologies/resource_download/d167805d-9a16-40b8-b3fb-123ac3edab20, (Accessed November 2018)